A SEARCH FOR VECTOR-LIKE LEPTONS IN ATLAS RUN 2 DATA

by

Bora Örgen

B.S., Physics, Boğaziçi University, 2018

Submitted to the Institute for Graduate Studies in
Science and Engineering in partial fulfillment of
the requirements for the degree of
Master of Science

Graduate Program in PHYSICS

Boğaziçi University

2021

ACKNOWLEDGEMENTS

Although I have been the one to document the study that is presented in this thesis, it would be impossible without our group members Prof. Veysi Erkcan Özcan, Assoc. Prof. N. Gökhan Ünel, Berare Göktürk, Assoc. Prof. Aytül Adıgüzel, Dr. Ümit Kaya and Prof. Saleh Sultansoy. I would like to thank them, not just for the knowledge they have shared but also for teaching me how to seek it on my own and improve myself.

I would also like to thank my friends who made my life so much better. First, I would like to thank Nedim Azgari, my long-time close friend. Without his encouragement, I would not have found the courage to follow my dreams to pursue a career in physics. Also, I would like to thank Efe Hamamcı. He has been quite the go-to guy when I needed to let off some steam. Although I have thanked Berare Göktürk for all the help she has given me, let me thank her again. Talking with her when I was stressed out instantly made me feel better.

I am also very grateful for my parents for providing me with the means to get as good an education as I got and the unwavering support they have provided.

Lastly, I would like to thank Elif Bayındır. She has been the joy of my life since the day I met her seven years ago. Living all these years together has been the happiest time of my life. I can't even put it into words how glad I am to have you.

ABSTRACT

A SEARCH FOR VECTOR-LIKE LEPTONS IN ATLAS RUN 2 DATA

The search for pair-produced heavy iso-singlet leptons predicted by Grand Unified Theory (GUT) based on group E_6 is detailed in this study. The discovery channel through which the search has been conducted is $pp \to L_e\bar{L}_e \to ZeW\nu_e \to 3l\,2j\,E_T^{miss}$. The data used in the study is the ATLAS Run 2 data which has an integrated luminosity of $\mathcal{L} = 139\,\text{fb}^{-1}$ from proton-proton collisions at 13 TeV center of mass-energy. A cut-based event selection has been performed to maximize signal to background yields. Exclusion limits without systematic uncertainties have been obtained, and the results have been found to be promising with the possibility to increase the lower mass limit of the heavy charged lepton to about 250 GeV from the previous limit of 100 GeV.

ÖZET

ATLAS RUN 2 DATASINDA VEKTÖR BENZERİ LEPTONLARIN ARANMASI

E_6 grubuna dayalı Büyük Birleşik Teori tarafından tahmin edilen çift üretilmiş ağır izo-tekil leptonların araştırılması bu çalışmada detaylandırılmaktadır. Aramanın keşif kanalı $pp \to L_e\bar{L}_e \to ZeW\nu_e \to 3l\,2j\,E_T^{miss}$'dır. Çalışmada kullanılan veriler, 13 TeV kütle merkezi enerjisindeki proton-proton çarpışmalarından elde edilen $\mathcal{L} = 139\,\text{fb}^{-1}$ toplam parlaklığa sahip ATLAS Run 2 verileridir. Sinyalin arka plan verimini en üst düzeye çıkarmak için kesim tabanlı bir olay seçimi gerçekleştirilmiştir. Sistematik belirsizlikler olmaksızın dışlama limitleri elde edilmiştir ve ağır yüklü leptonun alt kütle limitinin, önceki sınır olan 100 GeV'den yaklaşık 250 GeV'e çıkarılabileceğine dair umut vermiştir.

TABLE OF CONTENTS

LIST OF FIGURES

LIST OF TABLES

LIST OF SYMBOLS

A_μ	Electromagnetic Field
b, $\bar{b}$	Bottom Quark
c, $\bar{c}$	Charm Quark
d_0	Transverse Distance Between Track And The Beam Axis
d, $\bar{d}$	Down Quark
E_T	Transverse Energy
E_T^{miss}	Missing Transverse Energy
e, $\bar{e}$	Electron
H	Higgs Boson
j	Jet
ℓ	Lepton
L	Lagrangian
L_e	The Lightest Iso-singlet Lepton Predicted by E_6 GUT
$\mathcal{L}$	Luminosity
$\mathcal{L}_i$	Instantaneous Luminosity
m	Mass
p_T	Transverse Momentum
p	Proton
q	Quark
ΔR	Angular Distance
s, $\bar{s}$	Strange Quark
$\mathcal{S}$	Significance
$\mathcal{S}(E_T^{miss})$	Missing Transverse Energy Significance
t, $\bar{t}$	Top Quark
u, $\bar{u}$	Up Quark
$W^\pm$	W Boson With $+$ or $-$ Electrical Charge
z_0	Longitudinal Distance Between Track And Beam Axis
Z	Z Boson

γ^μ	Dirac Matrices
η	Pseudorapidity
θ	Polar Angle
θ_W	Weinberg Angle
μ, $\bar{\mu}$	Muon
ν_e, $\bar{\nu}_e$	Electron Neutrino
ν_μ, $\bar{\nu}_\mu$	Muon Neutrino
ν_τ, $\bar{\nu}_\mu$	Tau Neutrino
σ	Cross Section
τ, $\bar{\tau}$	Tau Lepton
ϕ	Azimuthal Angle
ψ	Fermion Field

LIST OF ACRONYMS/ABBREVIATIONS

ADL	Analysis Description Language
ATLAS	A Toroidal LHC ApparatuS
b	barn
BR	Branching Ratio
CERN	The European Organization For Nuclear Research
CMS	Compact Muon Solenoid
DAOD	Derived Analysis Object Data
GUT	Grand Unified Theory
HLT	High Level Trigger
IBL	Insertable B-Layer
ID	Inner Detector
IP	Interaction Point
LAr	Liquid Argon
LHC	Large Hadron Collider
LHCb	Large Hadron Collider beauty
LINAC	Linear Accelerator
LO	Leading Order
MC	Monte Carlo
NLO	Next to Leading Order
PDF	Parton Distribution Function
PS	Proton Synchrotron
PSB	Proton Synchrotron Booster
PV	Primary Vertex
QCD	Quantum Chromodynamics
RF	Radio Frequency
SCT	Semi-Conductor Tracker
SM	The Standard Model of Particle Physics
SPS	Super Proton Synchrotron

TRT	Transition Radiation Tracker
VLL	Vector Like Lepton

1. INTRODUCTION TO STANDARD MODEL AND BEYOND

The Standard Model of particle physics (SM) is the embodiment of our current knowledge about the elementary forces and particles of our universe. Although SM explains many physical processes with great accuracy, there are also many unanswered questions that are hot topics of research today.

1.1. Standard Model

SM is an effort to catalogue the fundamental building blocks of all the matter in the universe, which are named as elementary particles, and the forces with which they interact with one another. Since SM's inception 1970s, it has had many successful predictions, with the latest being the discovery of Higgs Boson [1,2] which has validated SM.

1.1.1. Elementary Particles

In SM, the elementary particles are divided into two main categories: fermions and bosons having half-integer and integer spin respectively. Fermions include leptons and quarks which, constitute ordinary matter. Bosons include force carriers and the Higgs Boson. Fermions follow Fermi-Dirac statistics and hence obey Pauli Exclusion Principle. On the other hand, bosons follow Bose-Einstein statistics. Categorization and many other properties of particles are given in Figure 1.1.

In the fermion family, there are 6 leptons and 6 quarks and their anti-particle counterparts which have the opposite physical charges but otherwise have the same attributes. Quarks and leptons are divided into three generations of one up-type quark, one down-type quark, one charged lepton and its corresponding neutrino.

The difference between two fermions of the same type is mass, while other properties such as spin or charge remain the same. The first generation fermions, being the lightest, are stable. Hence, ordinary matter around us is made up of the first generation charged leptons and quarks, namely electron e^-, up quark u and down quark d, which constitute protons and neutrons.

In SM, interactions are mediated by gauge bosons. The gauge boson of electromagnetism is the photon, and photons couple to every electrically charged particle. Thus, neutrinos do not feel the electromagnetic force since they lack an electric charge.

Strong interactions are mediated by massless gluon and couple to color charge. Quarks and gluons are the only elementary particles that have color charge and hence interact strongly. There are 3 color charges, namely red, green, and blue, but these are just naming conventions and have nothing to do with the everyday meaning of color. Every quark has color, and every anti-quark has anti-color. Quarks exhibit what is called a "color confinement", which essentially forbids any quark to be observed on its own. Instead, quarks and/or anti-quarks make up hadrons that are color neutral (white). A quark and an anti-quark with complementing colors can create a color-neutral bound state, but no configuration of two quarks or two anti-quarks can be in a bound state that is color neutral. Similarly, a three quark (anti-quark) bound state is possible with each quark (anti-quark) having different color (anti-color) charge, and no other color-neutral bound state configuration is possible that is composed of three quark, anti-quark combinations. Hadrons are divided into two groups based on their spin; those with integer spin are called mesons, and those with half-integer spin are called baryons. Mesons are usually made up of one quark and an anti-quark, whereas baryons are typically made up of three quarks or three anti-quarks.

Weak charged-current interaction is mediated by the W^+ and the W^- bosons, and weak neutral-current interaction is mediated by the Z boson. It is important to note that quark flavor change can only occur via weak charged-current interaction, and weak neutral-current interactions do not permit a flavor change in SM.

The only spin-0 (scalar) particle of SM is the Higgs boson. It is an excitation of the Higgs field, and interaction with this field is the process by which weak interaction gauge bosons acquire mass [3, 4].

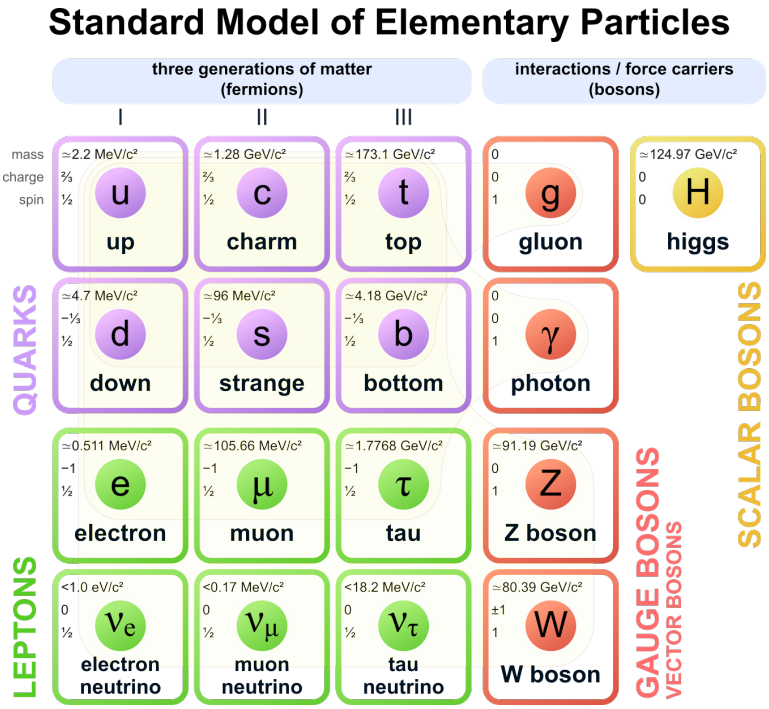

Figure 1.1. Mass, charge, spin and generation of elementray particles in SM [5]. The figure was created in 2019 so the masses and their errors may have changed. Up to date information can be found in [6].

Lagrangian of SM is based on a gauge group that is a direct product of three groups:

$$SU(3)_C \times SU(2)_L \times U(1)_Y \tag{1.1}$$

where, U and SU stands for unitary and special unitary group respectively and the groups that comprise the gauge group will be further discussed in the upcoming sections.

1.1.2. Electroweak Theory

Sheldon Glashow proposed that unification of electromagnetism and weak interaction is possible with 4 massless gauge bosons in his 1961 paper [7]. Independent from each other, Steven Weinberg in 1967 [8] and Abdus Salam in 1968 [9] incorporated the Higgs mechanism into Glashow's model. Glashow, Weinberg and Salam got the Nobel Prize for their contributions to the unification of electromagnetic and weak interactions in 1979 [10] following the discovery of neutral currents and measurement of parity violation in ee scattering.

The last two terms $SU(2)_L \times U(1)_Y$ in Equation (1.1) governs the Electroweak Theory. $W^1_\mu, W^2_\mu, W^3_\mu$ are the gauge bosons associated with $SU(2)_L$ and B_μ is associated with $U(1)_Y$. Coupling constants will be denoted as g and g' respectively throughout this section. L is the abbreviation of left and indicates that the symmetry applies to left-handed fermion fields. The weak isospin is conserved. Y in Equation (1.1) denotes the conserved quantity, hypercharge. The left-handed fermionic fields are doublets, whereas right-handed fermionic fields are singlets, and there are no right-handed neutrinos. The left-handed fermion fields transform depending on their generation i as;

$$\psi_i = \begin{pmatrix} \nu_i \\ l_i^- \end{pmatrix}, \begin{pmatrix} u_i \\ d_i' \end{pmatrix} \tag{1.2}$$

where, $d_i' = \sum_i V_{ij} d_j$ and V_{ij} is the element of Cabibbo-Kobayashi-Maskawa mixing matrix, also known as quark mixing matrix. $|V_{ij}|^2$ is related to the transition probability from q_j to q_i through weak interaction. Through the Brout-Englert-Higgs mechanism, the spontaneous symmetry of $SU(2)_L \times U(1)_Y$ breaks into $U(1)_{EM}$ which is the symmetry of electromagnetic interaction. Hence, W_μ gain mass.

The Lagrangian density for electroweak interaction after the symmetry breaking can be given as

$$\begin{aligned} L_{EW} = & \sum_i \bar{\psi}_i \left(i\partial\!\!\!/ - m_i - \frac{m_i H}{v} \right) \psi_i \\ & - \frac{g}{2\sqrt{2}} \sum_i \overline{\Psi}_i \gamma^\mu (1-\gamma^5)(T^+ W_\mu^+ + T^- W_\mu^-)\psi_i \\ & - e \sum_i Q_i \bar{\psi}_i \gamma^\mu \psi_i A_\mu \\ & - \frac{g}{2\cos\theta_W} \sum_i \bar{\psi}_i \gamma^\mu (g_V^i - g_A^i \gamma^5)\psi_i Z_\mu \end{aligned} \tag{1.3}$$

where, γ^μ are the Dirac γ-matrices, m_i is the fermions mass, v is the non-zero vacuum expectation value of Higgs Field, T^+ and T^- are weak isospin raising and lowering operators, $W_\mu^\pm \equiv \left(W_\mu^1 \mp i W_\mu^2\right)/\sqrt{2}$ are the charged weak boson fields, $e = g\sin\theta_W$ is the positron electric charge, Q_i is the electric charge of ψ_i divided by e, $A_\mu \equiv B_\mu \cos\theta_W + W_\mu^3 \sin\theta_W$ is the photon field, $\theta_W = \tan^{-1}(g'/g)$ is the Weinberg angle (also known as weak mixing angle), $Z_\mu \equiv -B_\mu \sin\theta_W + W_\mu^3 \cos\theta_W$ is the neutral boson field of weak interaction and finally $g_V^i \equiv t_{3L}(i) - 2Q_i \sin^2\theta_W$ and $g_A^i \equiv t_{3L}(i)$ are the vector and axial-vector couplings where $t_{3L}(i)$ is the weak isospin of i^{th} fermion.

1.1.3. Quantum Chromodynamics

$SU(3)_C$ component in Equation (1.1) is the Quantum Chromodynamics (QCD) part where C stands for the conserved quantum number, color. The Lagrangian density for QCD is given as

$$L_{QCD} = \sum_q \bar{\psi}_{q,a}(i\gamma^\mu \partial_\mu \delta_{ab} - g_s \gamma^\mu t_{ab}^C \mathcal{A}_\mu^C - m_q \delta_{ab})\psi_{q,b} - \frac{1}{4} F_{\mu\nu}^A F^{A\mu\nu} \tag{1.4}$$

where, g_s is the coupling constant for strong interaction, $\mathcal{A}_\nu^C$ is gluon field where C indicates which gluon out of eight types is considered, t_{ab}^C are known as Gell-Mann matrices, which are the generators of $SU(3)$.

$F^A_{\mu\nu} = \partial_\mu \mathcal{A}^A_\nu - \partial_\nu \mathcal{A}^A_\mu - g_s f_{ABC} \mathcal{A}^B_\mu \mathcal{A}^C_\nu$ in the last term is the field tensor where f_{ABC} represents the structure constants of $SU(3)$.

1.2. Beyond Standard Model

SM is a great achievement for the world of physics, but there are still many theoretical and experimental open questions that are not answered within SM. Some of these questions are listed below:

- Matter asymmetry stems from a simple question about why there is more matter than anti-matter in the observable universe [11] despite the fact that our current understanding predicts them to be created and destroyed almost equally.
- Gravity is not involved in SM, which prevents us from understanding the very early universe in a single framework. The "cosmological constant" problem gives a good example of how incompatible SM and experimental observations are when it comes to gravitational effects. The prediction based on SM is about 120 orders of magnitude higher than the experimental findings [12].
- Dark matter and dark energy, which are considered to make up about 95% of our universe, are not included in SM. Hence, SM only accounts for about 5% of the mass and energy in the universe, which is mostly baryonic matter [13].
- Hierarchy problem is about many orders of difference in masses and strength of forces such as gravity being in the order of 10^{24} weaker than the weak force. At the root of the problem lies the fact that the contribution of quantum loop corrections to the mass of Higgs is in the order of Planck mass of about $10^{19}\,\mathrm{GeV}$ and mass of Higgs boson is determined to be $125 \pm 0.14\,\mathrm{GeV}$ [14] in the latest measurements.

There are many theoretical endeavours to fill the holes in SM but GUT based on group E_6 will be the only beyond Standard Model (BSM) theory that will be covered in this work. As the electroweak theory unified electromagnetism and weak interaction, a GUT aims to unify QCD with electroweak theory.

This would be an amazing achievement and can potentially pave the way to the theory of everything by which all four fundamental forces are unified. The Georgi–Glashow model [15] was the first GUT, and it was based on $SU(5)$, which is the smallest simple Lie Group that contains the gauge group of SM given in Equation (1.1). The model predicts a proton decay lifetime that has not been experimentally observed, which rules out the initial model, but supersymmetric versions of it are yet to be ruled out. Although there have been many attempts to build a GUT, our focus in this work will be on a model based on the exceptional simple Lie Group E_6.

1.2.1. GUT Based on E_6

Gürsey, Ramond and Sikivie proposed in 1976 a GUT based on the exceptional simple Lie Group E_6 [16]. E_6 contains chiral fermions. In the most simplistic terms, this theory predicts a new quark and a charged lepton for each family. The lightest of the predicted iso-singlet lepton is denoted as L_e in this study. There are 3 decay channels for L_e: $W\nu_e$ controlled by mixing angle ϕ_L, Ze and He controlled by ϕ_R [17]. In our study, ϕ_L and ϕ_R are chosen to be equal. The Lagrangian density for iso-singlet L_e is given in Equation (1.5), which is followed by the Lagrangian density for iso-doublet in Equation (1.6). Details can be found in [18].

$$\begin{aligned} L_W &= -\frac{g}{\sqrt{2}}(V_{E\nu_l}\bar{E}\gamma^\mu P_L\nu_l W_\mu^- + V_{E\nu_l}^*\bar{\nu}_l\gamma^\mu P_L E W_\mu^+) \\ L_Z &= -\frac{gs_W^2}{c_W}\bar{E}\gamma^\mu E Z_\mu + \frac{8}{2c_W}(V_{E\nu_l}\bar{E}\gamma^\mu P_L\ell + V_{E\nu_l}^*\bar{l}\gamma^\mu P_L E)Z_\mu \\ L_\gamma &= e\bar{E}\gamma^\mu E A_\mu \\ L_H &= -\frac{gm_E}{2M_W}(V_{E\nu_l}\bar{E}P_L l + V_{E\nu_l}^*\bar{l}P_R E)H \end{aligned} \tag{1.5}$$

$$
\begin{aligned}
L_W &= -\frac{g}{\sqrt{2}}(\bar{E}\gamma^\mu N W_\mu^- + \bar{N}\gamma^\mu E W_\mu^+) - \frac{g}{\sqrt{2}}(V_{lN}\bar{l}\gamma^\mu P_R N W_\mu^- + V_{lN}^*\bar{N}\gamma^\mu P_R l W_\mu^+) \\
L_Z &= -\frac{g}{2c_W}([-1+2s_w^2]\bar{E}\gamma^\mu E + \bar{N}\gamma^\mu N)Z_\mu + \frac{g}{2c_W}(V_{lN}\bar{l}\gamma^\mu P_R E + V_{lN}^*\bar{E}\gamma^\mu P_R l)Z_\mu \\
L_\gamma &= e\bar{E}\gamma^\mu E A_\mu \\
L_H &= \frac{g m_E}{2M_W}(V_{IN}\bar{l}P_L E + V_{lN}^*\bar{E}P_R l)H
\end{aligned}
\tag{1.6}
$$

In this study, the search for L_e is being conducted through the discovery channel $pp \to L_e\bar{L}_e \to ZeW\nu_e \to 3l\,2j\,E_T^{miss}$. It is worth noting that there is flavor changing neutral current in the branch involving the Z boson, which is a distinct indication of physics beyond SM.

2. THE LHC AND THE ATLAS DETECTOR AT CERN

European Organization for Nuclear Research (CERN) is the world's largest particle physics research center. It is based near Geneva, Switzerland, right at the border between France and Switzerland. Having over 2600 personnel and over 11 thousand users from all over the world, it is a vast organization [19]. In the coming sections, the Large Hadron Collider (LHC) accelerator complex and the A Toroidal LHC Apparatus (ATLAS) detector are explained in detail.

2.1. LHC Accelerator Complex

CERN accelerator complex hosts many different accelerators accelerating different types of particles and collision detectors, as shown in Figure 2.1.

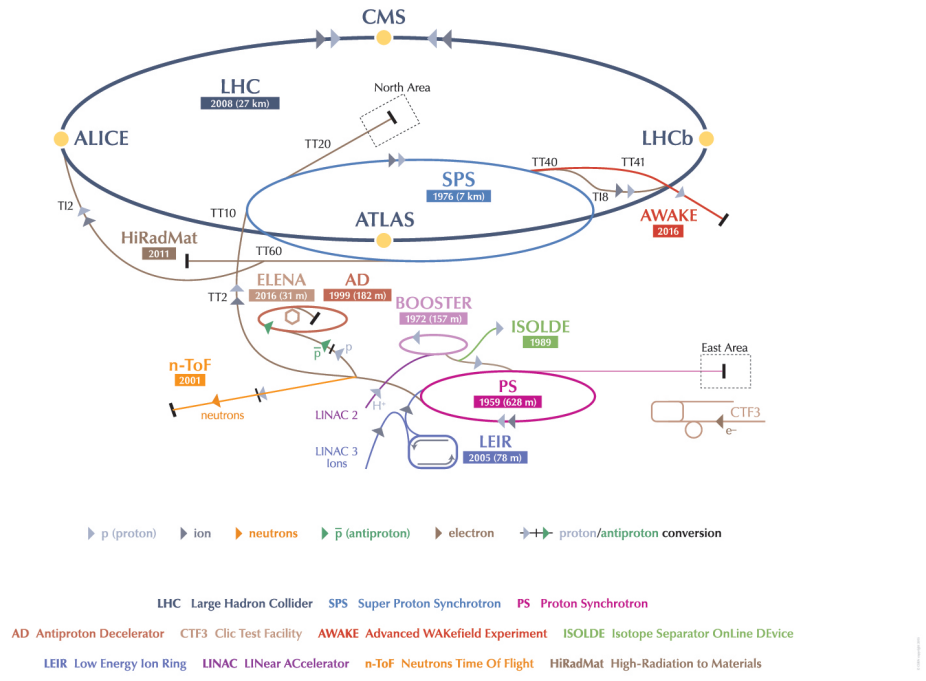

Figure 2.1. Parts that make up the CERN Accelerator Complex [20].

The LHC is the newest, most advanced accelerator added to the CERN accelerator complex. Particles are accelerated initially by other accelerators to specific energies and directed into the LHC to be further accelerated, as shown in Figure 2.1. Protons are accelerated to the final collision energies of 6.5 TeV by 8 superconducting radiofrequency cavities with oscillating electromagnetic fields at 400 MHz. Particles are kept in a circular orbit by applying a 7.7 T magnetic field provided by 1392 superconducting Nb-Ti dipole magnets, which operate at a temperature of 1.9 K. To maximize the number of collisions per bunch crossing, beams are focused by 392 quadrupole magnets. Essential parameters of LHC are given in Table 2.2.

Table 2.1. Kinetic energy gain of a proton as it is accelerated through CERN machines [21].

Accelerator	**Kinetic energy of a proton**
LINAC 2	50 MeV
PSB	1.4 GeV
PS	25 GeV
SPS	450 GeV
LHC	6.5 TeV

Starting operations in September of 2008 with a beam energy of 3.5 TeV and raising to 4 TeV afterwards, LHC collided protons until early 2013, named the Run 1 data-taking period. The LHC then entered into a shutdown phase where upgrades were implemented to increase the energy and rate of collisions. The shutdown was followed by the Run 2 data-taking period, starting in 2015 and ending in 2018.

There are 4 main detectors at the LHC: A Toroidal LHC ApparatuS (ATLAS), Compact Muon Solenoid (CMS), A Large Ion Collider Experiment (ALICE), and Large Hadron Collider beauty (LHCb). ATLAS and CMS are large general-purpose particle detectors. The upcoming chapters focus on the inner mechanisms of the ATLAS detector since the study uses data collected by the ATLAS detector.

ALICE is a detector specialized in measuring and analyzing lead-ion collisions and LHCb has been built to study the asymmetry between matter and antimatter present in interactions involving particles that contain the b quark.

Table 2.2. Technical parameters of the LHC [21]. The nominal energy of protons are kept at 6.5 TeV, but in fact the initial designed was to be 7 TeV.

Quantity	Number
Circumference	26659 m
Dipole operating temperature	1.9 K
Number of magnets	9593
Number of main dipoles	1232
Number of main quadrupoles	392
Number of RF cavities (per beam)	8
Nominal energy (protons)*	6.5 TeV
Nominal energy, proton collisions	13 TeV
Number of bunches per proton beam	2808
Number of protons per bunch (at start)	1.2×10^{11}
Number of turns per second	11245
Number of collisions per second	1 billion

2.1.1. Luminosity and Pileup

The number of collisions needs to be maximized to have better accelerator performance, and the parameter that defines it is instantaneous luminosity, $\mathcal{L}_i$. It is defined to be the ratio of event dN/dt rate to the cross-section σ of the interaction σ as

$$\mathcal{L}_i = \frac{1}{\sigma}\frac{dN}{dt}. \tag{2.1}$$

Instantaneous luminosity is usually measured in inverse barn b^{-1} per second, where one barn is equal to $10^{-28}\,\mathrm{m}^2$.

The instantaneous luminosity can be determined experimentally under the assumption that the beams have a Gaussian distribution as

$$\mathcal{L}_i = \frac{N_1 N_2 f N_b F}{4\pi\sigma_x\sigma_y} \tag{2.2}$$

where, N_1 and N_2 are the number of protons in the colliding bunches, f is the beam revolution frequency, N_b is the number of bunches in a beam, F is the correction factor due to crossing angle at the point of interaction, and finally σ_x, σ_y are horizontal and vertical spread of the beams. The number of collision events observed by the detector N for a time interval T can be found by rearranging Equation (2.1) as

$$N(T) = \epsilon\sigma\mathcal{L}(T) \tag{2.3}$$

where, ϵ is the efficiency of the detector and the integrated luminosity $\mathcal{L}$ is calculated as

$$\mathcal{L}(T) = \int_T \mathcal{L}_i dt. \tag{2.4}$$

As stated in Section 1.2.1, Run 2 data have a total integrated luminosity of $\mathcal{L} = 139\,\mathrm{fb}^{-1}$. The cumulative integrated luminosity as a function of time is given in Figure 2.2.

As a consequence of increasing luminosity to get more collisions, multiple collisions occur whenever two bunches of protons cross. This makes it hard to identify what the products of a single interaction are. This problem is referred to as pileup. Pileup can occur due to multiple proton-proton collisions in the same bunch crossing or interactions from previous or next bunch crossing interfere with the one of interest. To prevent the latter case, it is imperative to have a fast detector, and trigger response as the bunch crossings are only seperated by 25 ns. Figure 2.3 shows the number of events per bunch crossing increase as luminosity increases from year to year.

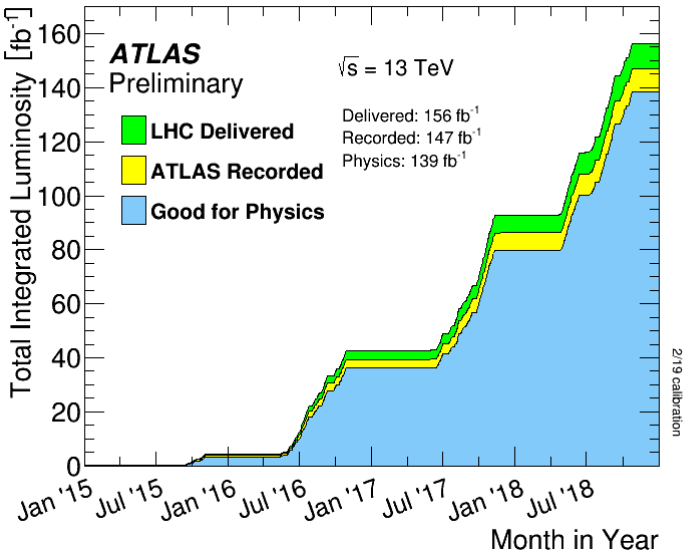

Figure 2.2. Total luminosity delivered to ATLAS versus time is shown in green for proton-proton collisions at the center of mass energy of 13 TeV during the 2015-2018 period [22]. The recorded part is shown in yellow, and the part that is declared to be good for physics searches is shown in blue.

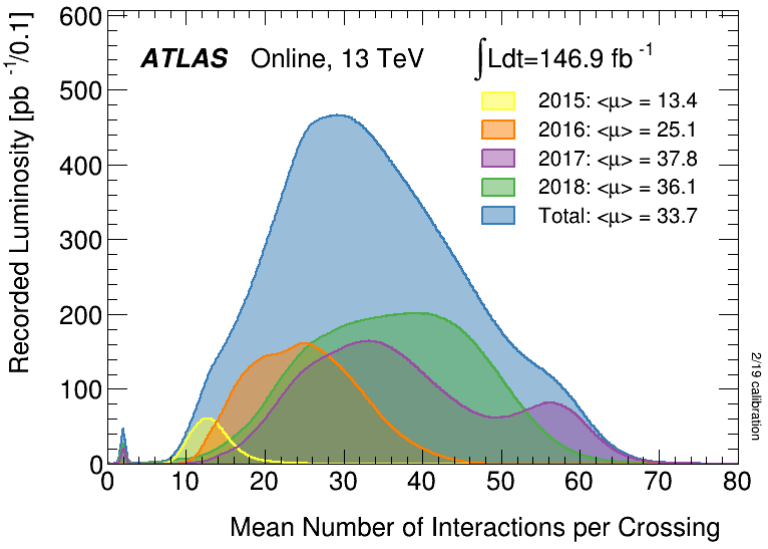

Figure 2.3. Luminosity-weighted distribution of the mean number of interactions μ per bunch crossing for Run 2 data. Mean μ is given for each year, and blue shaded part shows the total distribution of μ [23].

2.2. ATLAS Detector

The ATLAS detector is the largest general-purpose particle detector by volume on the LHC ring. It weighs over 7000 tons and has a cylindrical shape with a diameter of about 25 m, and a length of 44 m [24]. A computer generated image ATLAS detector is shown in Figure 2.4.

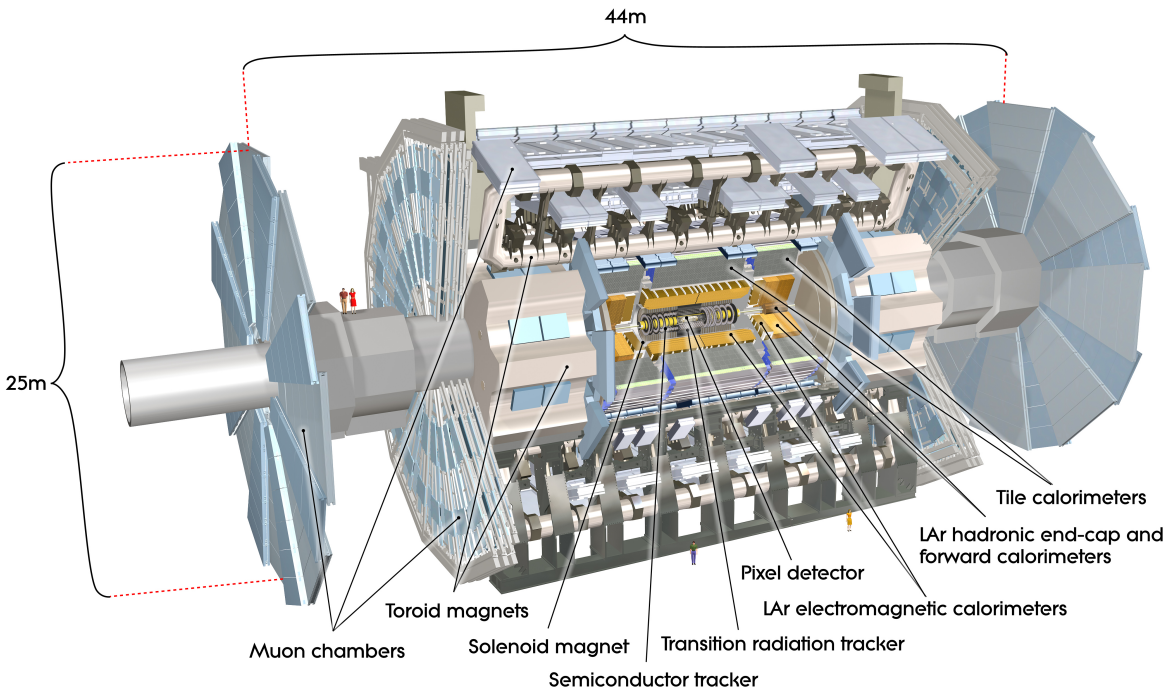

Figure 2.4. Computer generated image of the ATLAS detector as a whole [25].

There are many layers to ATLAS that are designed for specific functions. As particles move from the inner layers to the outer layers of ATLAS, they lose energy based on the properties of a given section. This is shown in Figure 2.5. Two additional design parameters are the available physical space and cost of construction of the detector, which ultimately restricts the detection quality we can get from the machine. Also, the parts of ATLAS that are close to the interaction point (IP), which is the point where we expect the bunches cross each other, need to be resistant to high particle flow rates for the duration of a data-taking run.

Another goal of the ATLAS collaboration is to capture all the resultant particles of the collisions, which requires the detector to be able to detect particles moving in all directions. Hence, ATLAS provides nearly 4π coverage in the solid angle.

In a general purpose detector such as ATLAS, each particle leaves its own signature. Charged particles are deflected and leave an ionization trail in the inner tracker. Muons additionally leave deflected ionization trails in the muon system. Photons and electrons are stopped via showering in the electromagnetic calorimeter. Hadrons shower in the electromagnetic and hadronic calorimeters. Neutrinos essentially do not interact with the detector and hence do not leave a trace.

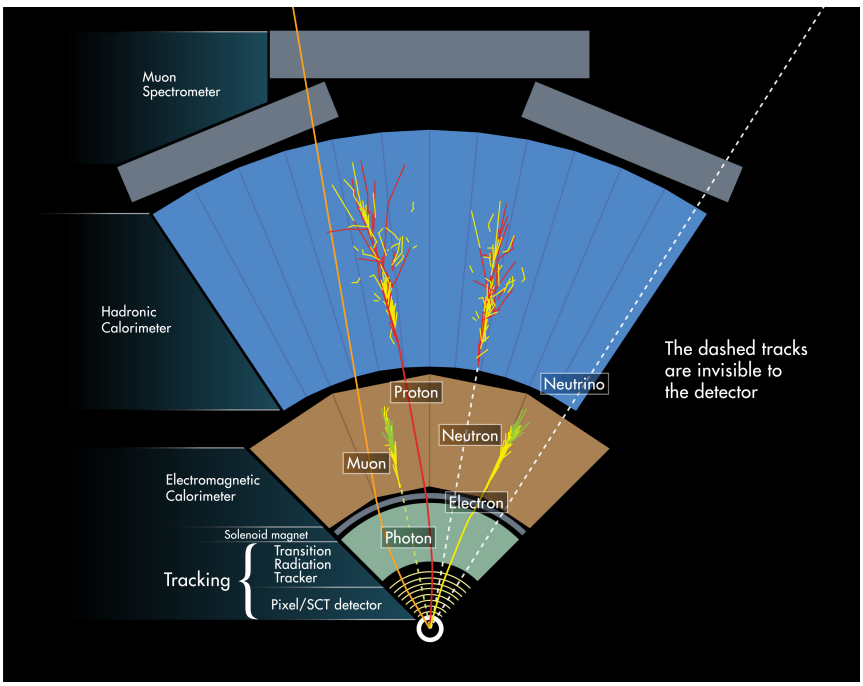

Figure 2.5. Particles leave tracks and deposit their energies depending on their interactions with various layers of the detector [26].

2.2.1. Coordinate System

The center of the detector, IP, is chosen to be the origin of the coordinate system. The direction of the beam serves as the z-axis. From IP, the y-axis points upwards, and the x-axis points to the centre of the LHC ring.

The azimuthal angle ϕ is measured around the beam axis, and the polar angle θ is measured from the beam axis. A schematic of the coordinate system is given in Figure 2.6.

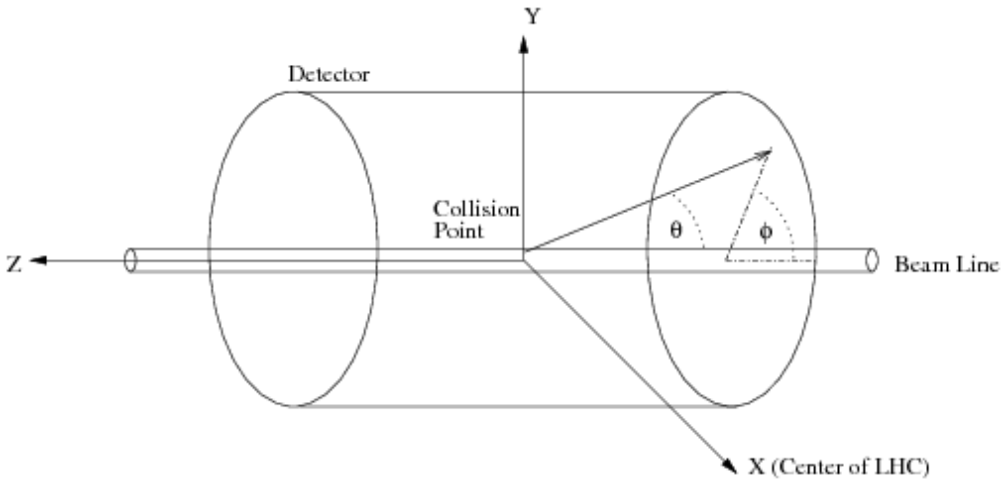

Figure 2.6. Illustration of the ATLAS and CMS coordinate systems. In this study, collision point is refered to as the IP [27].

The rapidity is defined as

$$y = \frac{1}{2} \ln \left(\frac{E + p_z}{E - p_z} \right) \tag{2.5}$$

where, E is the energy of the particle, and p_z is the longitudinal momentum. Since the collision products are very energetic, we can assume those particles to be relativistic and assume $pc >> mc^2$ to get an approximate value for rapidity by calculating pseudorapidity η as

$$\eta = -\ln \left(\tan \left(\frac{\theta}{2} \right) \right). \tag{2.6}$$

The angular distance between particles $\Delta R = \sqrt{\Delta\eta^2 + \Delta\phi^2}$ is Lorentz invariant for relativistic particles.

2.2.2. Inner Detector

The ATLAS Inner Detector (ID) [28–30] consists of four parts. First comes the Insertable B-Layer (IBL) which is the closest detector to the IP. The pixel detector envelopes the IBL. After pixel detector comes the silicon strip (SCT) detector, which surrounds the pixel detector. At the outermost layer, we have the transition radiation tracker (TRT). These layers can be seen in Figures 2.7 and 2.8. The entire ID is immersed in a uniform 2 T magnetic field generated by a central superconducting solenoid. The particles' momenta are then calculated by the curvature of their tracks in the magnetic field, and the sign of a particle's charge is discerned by which way the particle curves. ID covers a range of $|\eta| < 2.5$ and can record objects with p_T higher than 0.4 GeV.

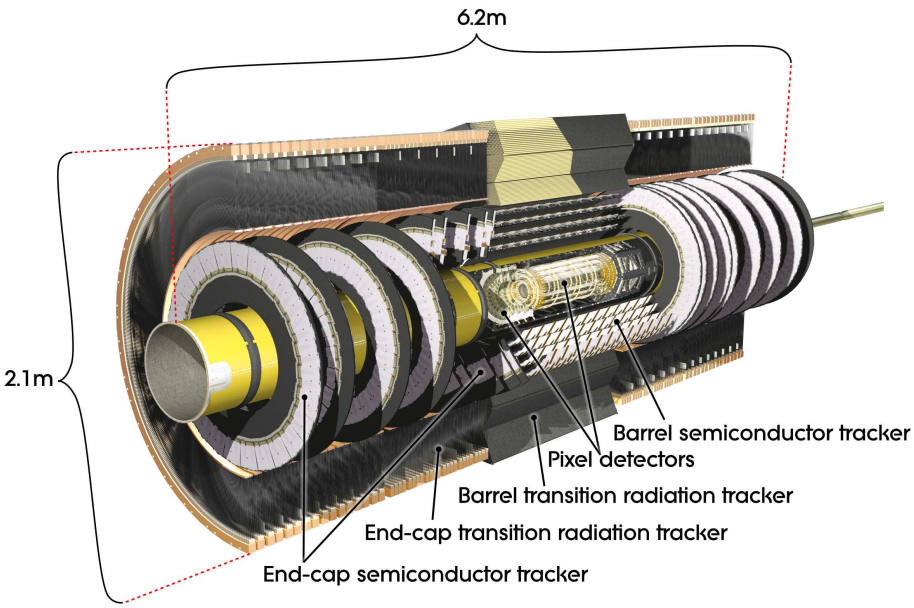

Figure 2.7. Cross-section of the ATLAS inner detector [31].

2.2.2.1. Insertable B-Layer. The IBL is the first layer collision products go through, and it consists of 224 modules amounting to a total of six million pixels. It was installed in May 2014 with the primary goal of improving the tracking and vertex reconstruction [32]. The IBL is placed at 33.25 mm from the IP.

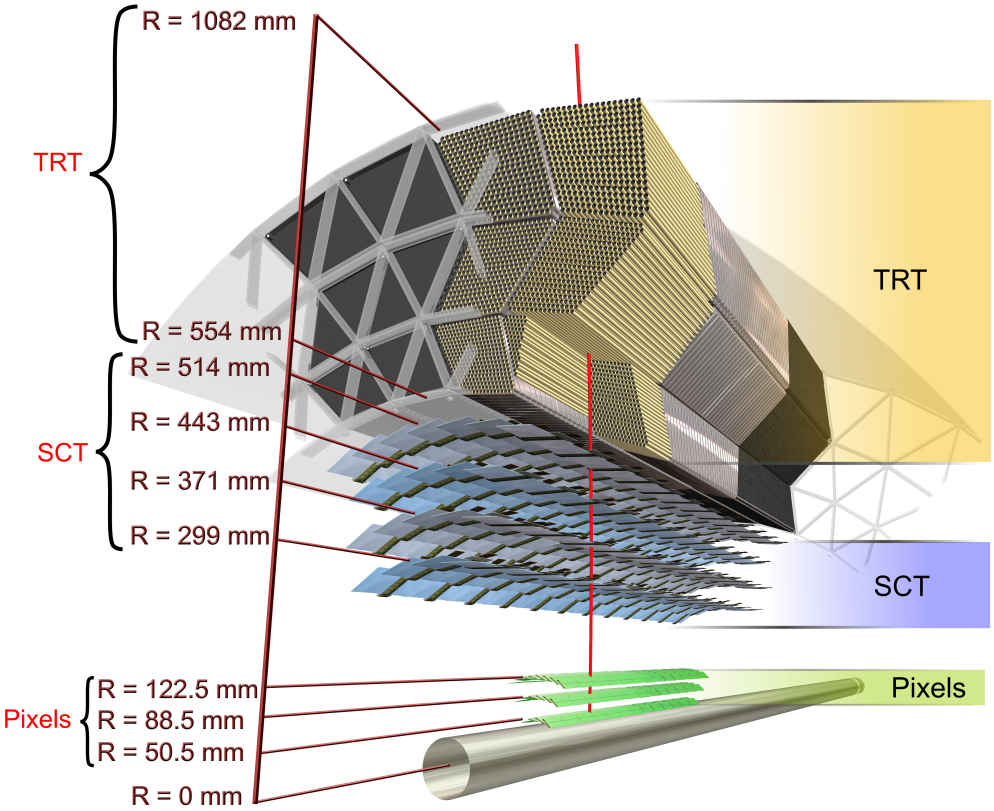

Figure 2.8. A 3D visualization of the ID, showing each of its components [31].

2.2.2.2. Pixel Detector. Pixel detector consists of 3 barrel and 3 end-cap layers of silicon semi-conductor pixel sensors. The pixel detector has 1744 modules with about 80 million pixels. Spatial resolution of Pixel Detector is 8 μm in the transverse direction and 75 μm at the end-caps along the beam pipe [33]. The pixel detector has three layers at 50.8, 88.5 and 122.5 mm from the interaction point and three disks at the ends.

2.2.2.3. Semi-conductor Tracker. The SCT is also made out of silicon semi-conductor sensors. In contrast to the pixel detector, the SCT does not have pixels, but 80 μm spaced microstrips [34]. The single plane resolution of SCT is about 17 μm in the transverse direction and 580 μm in the longitudinal direction.

2.2.2.4. Transition Radiation Tracker. The final layer of the ID is the TRT. There are over 50000 straws of 144 cm in the barrel part and over 120000 straws of 37 cm in each of the end-caps [35]. These straws consist of layers made out of different materials, as can be seen in Figure 2.9. Inside of the straws are filled with a gaseous mixture mostly consisting of Xe and a gold plated wire stretches across the straw to act as the anode. The wire collects charges generated by ionization due to passing charged particles or by x-ray photons coming from the transition radiation created by the final products of the collisions. The transition radiation energy is inversely proportional to the mass of a particle, so light electrons can be distinguished from hadrons such as pions. The outer walls are kept at a negative potential of $-1.5\,\mathrm{kV}$ to act as the cathode.

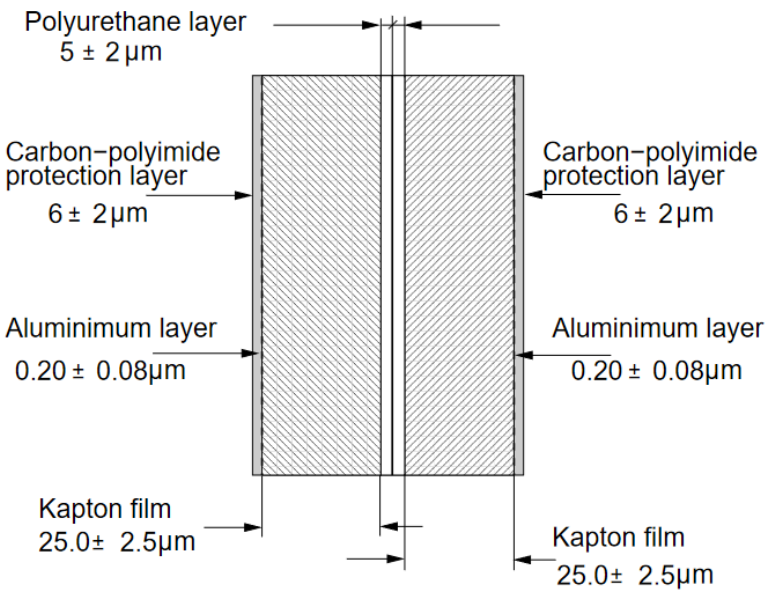

Figure 2.9. Design of the TRT straw wall [35].

2.2.3. Calorimeters

After going through ID, particles reach electromagnetic and hadronic calorimeters. The purpose of the calorimeters is to measure the energies of the particles which interact electromagnetically or strongly. To cover the whole solid angle, they are divided into a barrel and two end-cap parts. The calorimeter schematic is given in Figure 2.10.

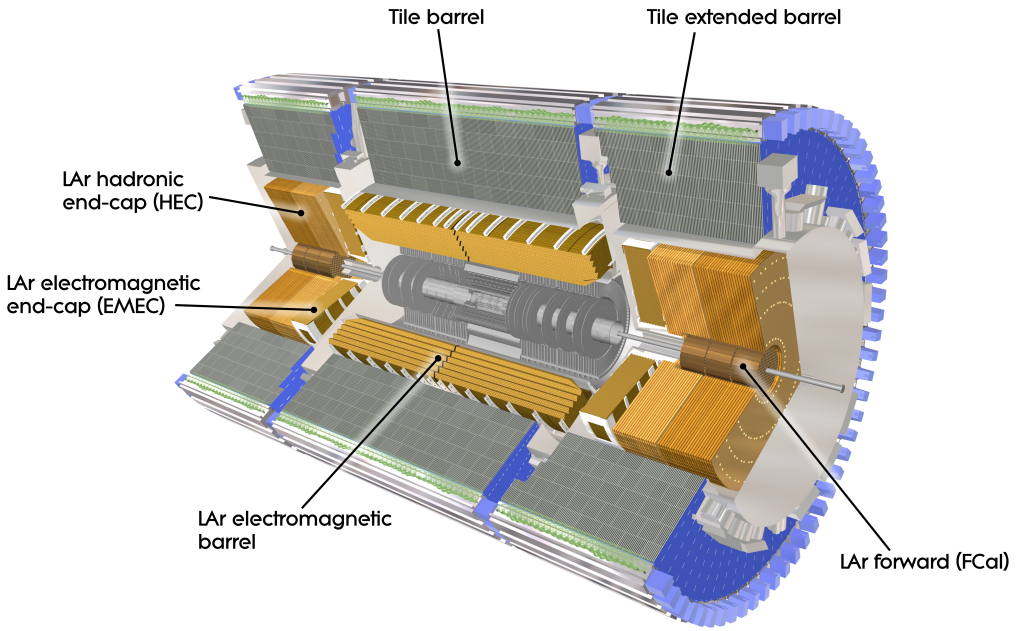

Figure 2.10. Computer generated image of the ATLAS calorimeter [36].

2.2.3.1. Electromagnetic Calorimeter. The depth of the electromagnetic calorimeter [37] is chosen so that all the energy of electromagnetic showers from electrons and photons are contained in this part of the calorimeter. The electromagnetic calorimeter is a lead-Liquid Argon (LAr) sampling calorimeter which means that the material that produces the particle shower is not the same as the material that measures the deposited energy. Lead parts act as energy absorber and produce photons due to bremsstrahlung. The accordion shape of the calorimeter adds several active layers while still ensuring full solid angle coverage. In the next layers with liquid argon gas, the ionized particles due to showers are recorded. The barrel covers $|\eta| < 1.475$ while end-caps cover $1.375 < |\eta| < 3.2$. The second sampling region has a granularity of $\Delta\eta \times \Delta\phi = 0.025 \times 0.025$. The EM calorimeter has a designed energy resolution of $\frac{\sigma_E}{E} = \frac{10\%}{\sqrt{E}} \oplus 0.7\%$ [38].

2.2.3.2. Hadronic Calorimeter. Ideally, the hadronic calorimeter, together with the electromagnetic calorimeter [39], should be able to contain the energy of showers from hadrons.

The hadronic calorimeter at ATLAS is a tile calorimeter consisting of repeating 14 mm steel plate absorbers and 3 mm scintillators which can be seen in Figure 2.11. Pseudorapidity of $0 < |\eta| < 1.7$ is covered by the tile calorimeter. A copper/LAr sampling calorimeter (HEC) and a copper-tungsten/LAr sampling calorimeter (FCal) extends the η coverage by $1.5 < |\eta| < 3.2$ and $3.1 < |\eta| < 4.9$ respectively. The hadronic calorimetry has a resolution of $\frac{\sigma_E}{E} = \frac{50\%}{\sqrt{E}} \oplus 3\%$ at the barrel and end-cap [38].

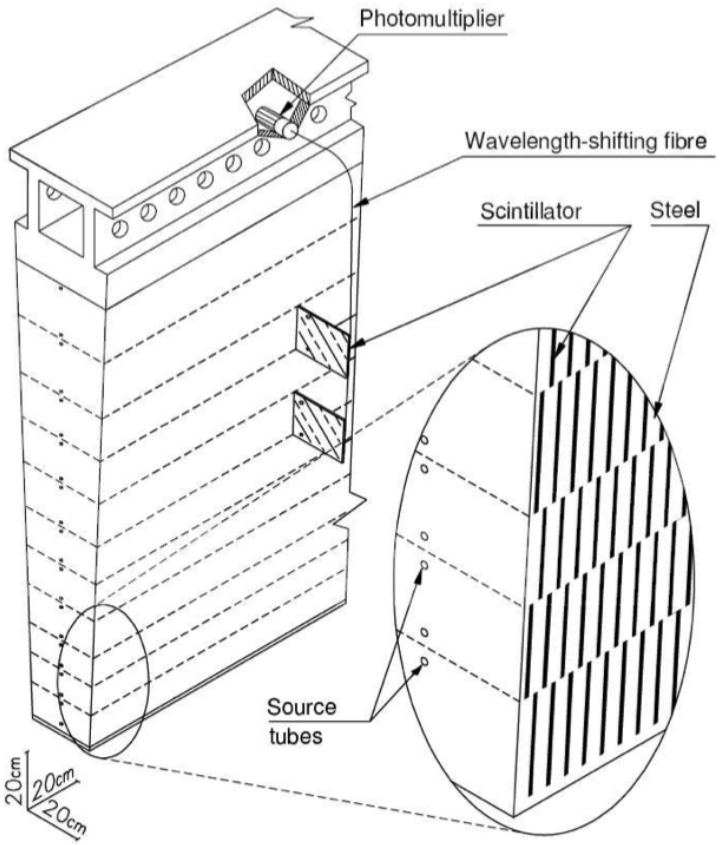

Figure 2.11. Sketch of a barrel module in the Tile Calorimeter [38].

2.2.3.3. Forward Calorimeter. To ensure full solid angle coverage, forward electromagnetic and hadronic calorimeters are added despite having a much lower resolution. It covers forward region of $3.1 < |\eta| < 4.9$. One side benefit to having a forward calorimeter is that it limits the background particles from reaching the muon system. Forward calorimeter has an energy resolution of $\frac{\sigma_E}{E} = \frac{100\%}{\sqrt{E}} \oplus 10\%$ [38].

2.2.4. Muon System

The muon system [40,41] is the outermost and largest part of the ATLAS detector, and a sketch of it can be found in Figure 2.12. The main purpose of the muon system is to detect tracks of muons. Ideally, only neutrinos and muons should be able to reach here. Muons with transverse momenta of at least 3 GeV are detected with Muon System. Barrel section covers $|\eta| < 1.05$ and three layers along with the endcaps cover $1.05 < |\eta| < 2.7$. Toroid magnets of the muon system create a magnetic field from 1 to 2 T. Knowing the magnetic field strength, the momentum of muons are calculated. There are four different types of detectors in the muon system: Monitored Drift Tubes [42] and Cathode Strip Chambers [43] are used for tracking in $|\eta| < 2.7$ and $2.0 < |\eta| < 2.7$ regions respectively. Resistive Plate Chambers [44] and Thin Gap Chambers are used for triggering in $|\eta| < 1.05$ and $1.05 < |\eta| < 2.4$ regions respectively. Transverse momentum resolution is $\sigma_{p_T}/p_T = 10\%$ at p_T =1 TeV [38].

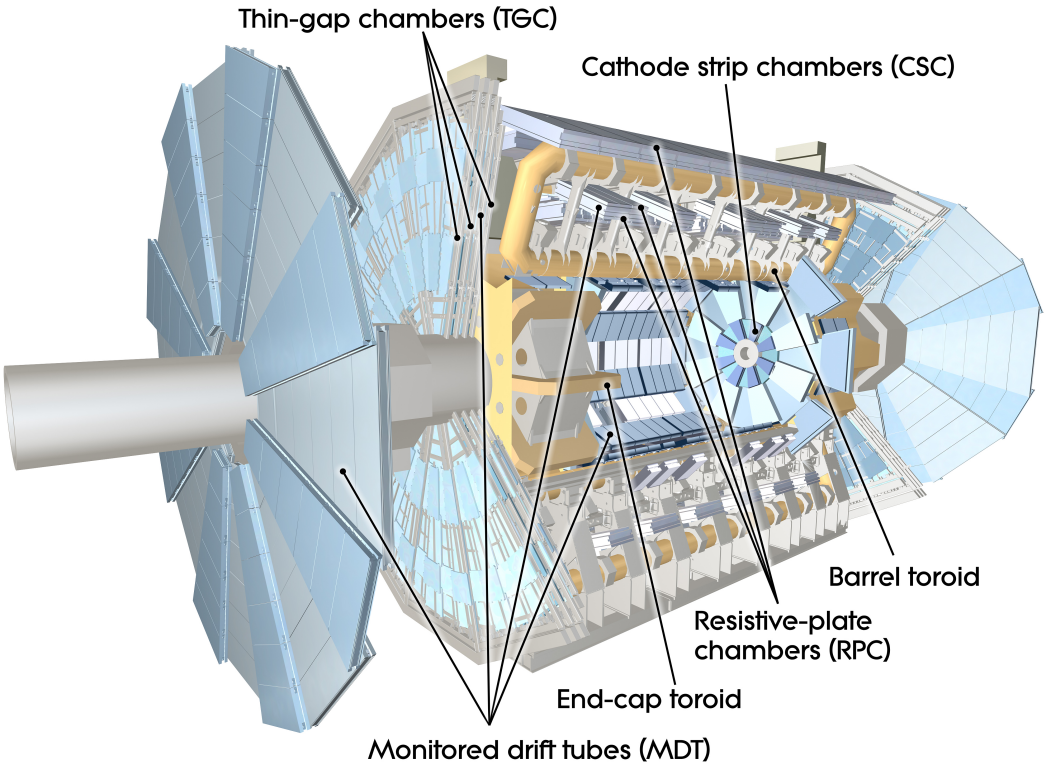

Figure 2.12. Computer generated image of the ATLAS Muons subsystem [45].

2.2.5. Trigger System

Considering the bunch crossing rate of 40 MHz in the LHC and the fact that recording an event needs about an MB of disk space, it is not feasible to record each and every collision for later reconstruction and inspection. This problem is addressed by the trigger system, which in essence tries to select the events that can help us make new observations. The reduction from the available events to the actual recorded events are made in two steps by The ATLAS Trigger and Data Acquisition System (TDAQ). First is the hardware-based Level-1 (L1) trigger and second is the single software-based High-Level Trigger (HLT).

The L1 trigger uses costly specialized electronics, and goes through the coarse information about the events. L1 trigger quickly decides which events are to be passed to the HLT. L1 trigger processes data from the calorimeters and the muon detectors and looks for signatures such as large electromagnetic energy deposits or high-p_T muon tracks [46]. The L1 trigger reduces the readout event rate to less than 100kHz.

Events that pass the L1 trigger are then processed by the HLT with full detector information. HLT is a software-based trigger that operates on a large farm of computer processors that fully reconstructs the events. The decision about whether the event is to be saved is made within a second [46]. After the HLT, the readout event rate is reduced to about 1 kHz.

2.2.6. Data Framework

It is not practical to work with all the data recorded by the ATLAS detector for an analysis, so it is preferable to work on a subset that has minimal information unrelated to the analysis of interest. Data stored after HLT have a size in the order of PB. From this data, Analysis Object Data (AOD) are created after the addition of tracks, hits and trigger information. This format is still too large to work with, so Derived Analysis Object Data (DAOD) are produced to the needs of specific analyses.

Data reduction in the derivation step is made through three different methods: skimming, thinning and slimming. Skimming is removing whole events based on criteria such as having at least an electron in each event. Slimming removes redundant objects within events, such as removing the photon objects from each event if they are not used in the analysis. Thinning removes object variables unnecessary to the analysis. After derivation step, n-tuples are created from the DAOD's which are much smaller than DAOD's (MB to GB in size). An n-tuple is an ordered list with n elements, and final analysis are done using these. These element hold the recording of an event, such as the number of electrons. Data flow from detector data to n-tuples for the analysis stage is given in the left branch of Figure 2.13.

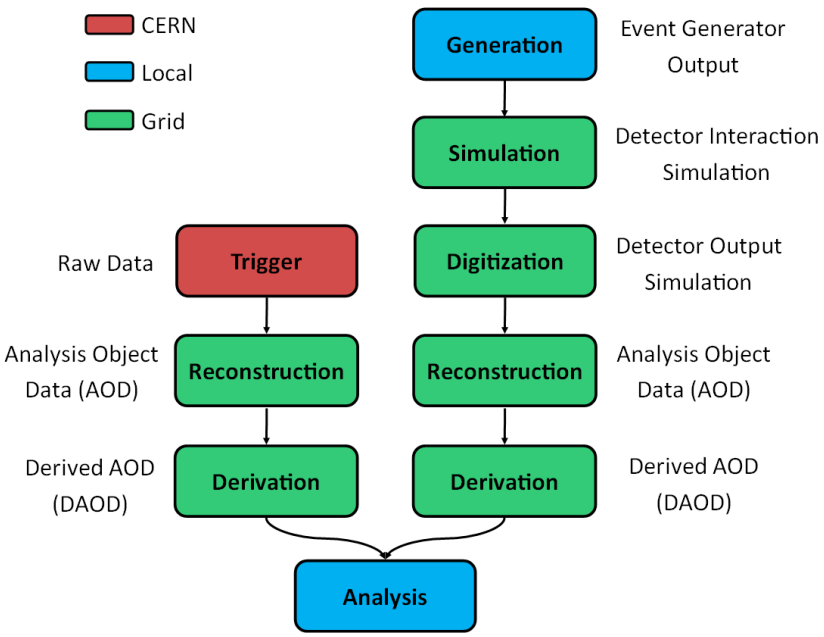

Figure 2.13. ATLAS data types for both detector data and Monte Carlo simulations.

The right branch in the Figure 2.13 shows the flow of creation of a Monte Carlo (MC) simulation. These are simulations of collisions that are expected to happen within SM or any interaction beyond SM. The event generation step is done by an event generator such as CompHEP [47] or MadGraph5 [48]. Then comes the hadronization, fragmentation and showering simulation, which is done by some software such as PYTHIA [49].

Finally, produced events interact with the detector in a simulation software such as Delphes [50] for fast simulation or Geant4 [51] for full simulation of the detector response. After this point, the road to n-tuples is the same as the data obtained from the ATLAS detector.

2.2.7. Object Reconstruction

The objects leave marks as they travel through the ATLAS detector, and from these marks, objects are reconstructed and classified. The final state of this analysis only has electrons, muons, jets and missing transverse energy E_T^{miss}, so the remaining sections will focus on their reconstruction processes. By connecting the hits in different layers, tracks can be reconstructed. All tracks need to have a $p_T > 400\,\text{MeV}$ and $|\eta| < 2.5$. Two parameters of tracks are d_0 and z_0, where d_0 is the transverse impact parameter, and z_0 is the longitudinal impact parameter.

2.2.7.1. Electrons. Electrons are tracked by the ID and deposit a significant amount of energy when passing through the electromagnetic calorimeter. The information coming from both ID and electromagnetic calorimeter are then used to reconstruct the electrons, but energy leakage to hadronic calorimeter is also taken into consideration to improve performance. Figure 2.14 shows an exemplary path of an electron as it travels through the detector. Initially, a sliding window with a size of 3×5 in granularity of electromagnetic calorimeter, $\Delta\eta \times \Delta\phi = 0.025 \times 0.025$, is used to search for the energy deposit clusters due to passing electrons. If the total cluster transverse energy is above 2.5 GeV, then that cell is marked as a seed, and a cluster is formed around it by an algorithm [52]. This algorithm has an efficiency of 95% at E_T =7 GeV and higher than 99% when E_T >15 GeV. Track candidates are fit to be either a pion or an electron by the ATLAS Global χ^2 –Track Fitter [53]. If a track has more than four precision hits and is loosely associated with an electron cluster, they are refit using an optimised Gaussian Sum Filter [54]. This method accounts for the non-linear bremsstrahlung effects.

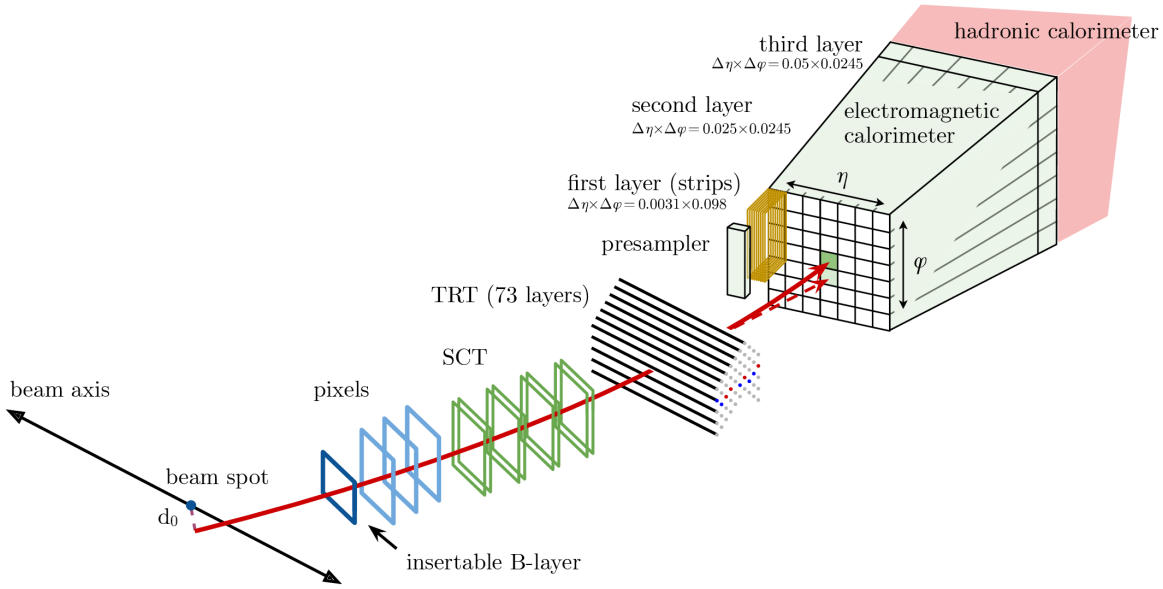

Figure 2.14. A schematic illustration of the path of an electron through the detector as it passes through different detector parts [55].

Electrons in the transition region $1.37 < |\eta| < 1.52$ are vetoed due to calorimeter being obstructed by the support tubes. The matched tracks are required to originate from the primary vertex (PV) with $d_0/\sigma_{d_0} > 5$ and $|z_0 \sin\theta| < 0.5\,\text{mm}$ and thus, background contamination by secondary particles are mostly prevented.

Three levels of identification operating points are typically provided for electron ID. These are Loose, Medium, and Tight, with each one more exclusive and less misidentification prone than the previous one. Although identification efficiency of Loose is the highest compared to the others, Tight ones are much less likely to be misidentified, as can be seen in Figure 2.15.

Based on the isolation of track and calorimetric signature, three categories are LooseTrackOnly, FixedCutLoose and FixedCutTight. These isolation requirements are expected of electrons so that they can be discriminated whether they have originated from the PV or from a secondary decay of a particle (jets in most cases) originating from PV. These criteria depend on $p_T^{varcone20}$ and $E_T^{varcone20}$ isolation requirements.

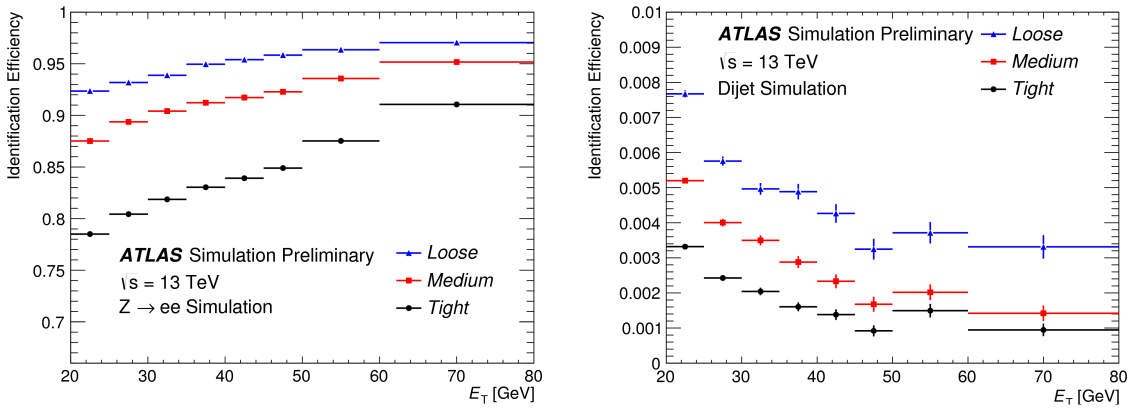

Figure 2.15. Left plot shows electron identification efficiencies in $Z \to ee$ events as a function of transverse energy. Right plot shows electron misidentification efficiencies in $Z \to ee$ events as a function of transverse energy [56].

$E_T^{varcone20}$ is calculated by summing the E_T of all topologically connected clusters within $\Delta R < 0.2$ with the exception of electron E_T. $p_T^{varcone20}$ is calculated in a similar manner as summing all p_T of the tracks in a cone of $\Delta R < \min((10\,\text{GeV})/(p_T \text{ of } e), 0.2)$ around the electron excluding p_T of electron. During this study, FixedCutLoose isolation criteria is used which requires electron candidates to have $E_T^{varcone20}/(p_T \text{ of } e) < 0.2$ and $p_T^{varcone20}/(p_T \text{ of } e) < 0.15$.

2.2.7.2. Muons. In addition to the ID signature, muon reconstruction depends on the dedicated muon system. The track reconstruction has four different methods depending on which subdetectors are involved in the reconstruction. The method involving the most reliable subdetectors are preferred when both methods tag the muon. As was the case with electrons, there are four categories of muons based on the identification criteria [41]. The first three of these criteria are Loose, Medium to Tight muons. From Loose to Tight, selection criteria demands are higher and hence tagged muons are purer at the expense of efficiency. The last category is HighpT muons, and muons in this category have the best momentum resolution where muon $p_T > 100\,\text{GeV}$. Table 2.3 shows efficiency and misidentification percentages based on the given identification classes.

Table 2.3. Efficiency of muons from W decays, ϵ_{μ}^{MC}, and hadrons decaying in flight to be identified as muons originating from PV, $\epsilon_{Hadrons}^{MC}$, obtained using a MC sample [41].

	$4 < p_T < 20\,\text{GeV}$		$20 < p_T < 100\,\text{GeV}$	
Selection	$\epsilon_{\mu}^{MC}[\%]$	$\epsilon_{Hadrons}^{MC}[\%]$	$\epsilon_{\mu}^{MC}[\%]$	$\epsilon_{Hadrons}^{MC}[\%]$
Loose	96.7	0.53	98.1	0.76
Medium	95.5	0.38	96.1	0.17
Tight	89.9	0.19	91.8	0.11
High-pT	78.1	0.26	80.4	0.13

Like the isolation requirements for electrons, muons have four categories depending on the calorimeter and track isolation. They can be ordered in increasingly more isolated categories as LooseTrackOnly, FixedCutTightTrackOnly, FixedCutLoose and FixedCutTight. These also depent on $p_T^{varcone20}$ and $E_T^{varcone20}$ isolation requirements where $E_T^{varcone20}$ reqirement is the same as electron. The only difference in muon $p_T^{varcone20}$ calculations is the change in the cone to $\Delta R < \min((10\,\text{GeV})/(p_T \text{ of } \mu), 0.3)$ around the muon track. In this study, FixedCutTightTrackOnly isolation criteria was used which requires $p_T^{varcone20} < 0.60$.

2.2.7.3. Jets. As quarks and gluons shoot out after the high energy collision, they produce particle showers by fragmentation and hadronization, and these showers are called jets. The jets deposit their energy to the hadronic calorimeter. The jets are formed into topological clusters [57] and reconstructed by the anti-k_t algorithm [58]. Jet reconstruction also involves reconstructing the particle shower's total energy. The jet-vertex-tagger technique [59] uses tracking and vertex information to remove the pileup jets effectively.

2.2.7.4. Missing Transverse Energy. The total energy of the particles in the transverse plane for each interaction are added together, and this value is named as missing transverse energy, E_T^{miss}.

The expectation value would be zero if the magnitude and direction of every particle's energy could be measured without any errors since the initial proton beams do not have any transverse energy. So, E_T^{miss} carries information about the particles that do not leave a mark in the detector, most notably the neutrinos. E_T^{miss} is calculated by the magnitude of the vector sum of all transverse energies as

$$E_T^{miss} = |\mathbf{E}_T^{miss,e} + \mathbf{E}_T^{miss,\gamma} + \mathbf{E}_T^{miss,\tau} + \mathbf{E}_T^{miss,jets} + \mathbf{E}_T^{miss,\mu} + \mathbf{E}_T^{miss,soft}| \tag{2.7}$$

where, each $\mathbf{E}_T^{miss,i}$ is the negative of the vector sum of all transverse momenta of i-type particle. The last term is for the reconstructed tracks that are not associated with any hard object, such as electrons or muons. E_T^{miss} can also be expressed by knowing the missing energy components in x and y directions as

$$E_T^{miss} = \sqrt{(E_x^{miss})^2 + (E_y^{miss})^2}. \tag{2.8}$$

Another parameter that will be used in this study is the missing transverse energy significance $\mathcal{S}(E_T^{miss})$. It can be calculated as

$$\mathcal{S}(E_T^{miss}) = E_T^{miss}/\sqrt{H_T} \tag{2.9}$$

where, H_T is the scalar sum of all transverse momenta of hard objects.

2.2.7.5. Overlap Removal. There is a chance that a detector signal satisfies identification criteria of more than one objects and results in multiple object reconstruction. The overlap removal procedure tries to reduce the number of reconstructed objects from a detector signal to just one. Such suspicious objects are removed by following some rules [60] to minimize this probability. An example could be that the removal of the jet is advised if there is an electron within an angular distance of $\Delta R < 0.2$. The tool developed by ATLAS is used to remove overlap [61].

3. THE SEARCH FOR E_6 ISO-DOUBLET LEPTONS

In this section, the search for the iso-singlet lepton predicted by E_6 GUT through the channel $pp \to L_e\bar{L}_e \to ZeW\nu_e \to 3l2jE_T^{miss}$, as shown in Figure 3.1, is discussed. The search is conducted on data recorded by the ATLAS detector from 2015 to 2018, which is called the Run2 data and has a total integrated luminosity of $139.9fb^{-1}$. During this period, LHC was colliding protons at a center of mass energy of $\sqrt{s} =$ 13 TeV.

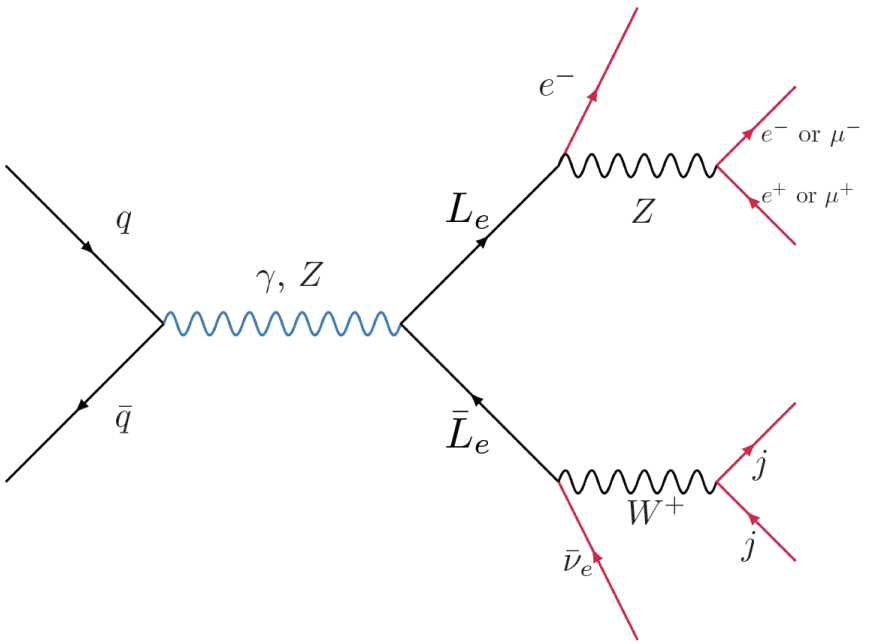

Figure 3.1. Pair production of E_6 isodoublet leptons L_e, their decay into $W\nu_e$ and Ze. Decay products of W are 2 jets and decay products of Z are either an electron, positron pair or a muon, anti-muon pair.

Total number of expected signal events for a given rest mass m_{L_e} of L_e can be calculated as

$$\sigma_{L_e\bar{L}_e} \times \mathcal{L} \times 2 \times BR(L_e \to Ze) \times BR(L_e \to W\nu) \times BR(W \to jj) \times BR(Z \to ee||\mu\mu) \tag{3.1}$$

where, $\sigma_{L_e\bar{L_e}}$ is the pair production cross-section of L_e, $\mathcal{L}$ is the integrated luminosity and BR is the abbreviation of "branching ratio", which is basically the relative decay probability of a certain decay. While $BR(L_e \to Ze)$ and $BR(L_e \to W\nu)$ depend on the rest mass of L_e, $BR(W \to jj) = 0.674$ and $BR(Z \to ee\, or\, \mu\mu) = 0.0673$ are set in SM [6]. The factor of 2 is there to account for the two ways the decay would result in one W and one Z boson final state. In Table 3.1, number of expected signal events for rest masses of interest are given.

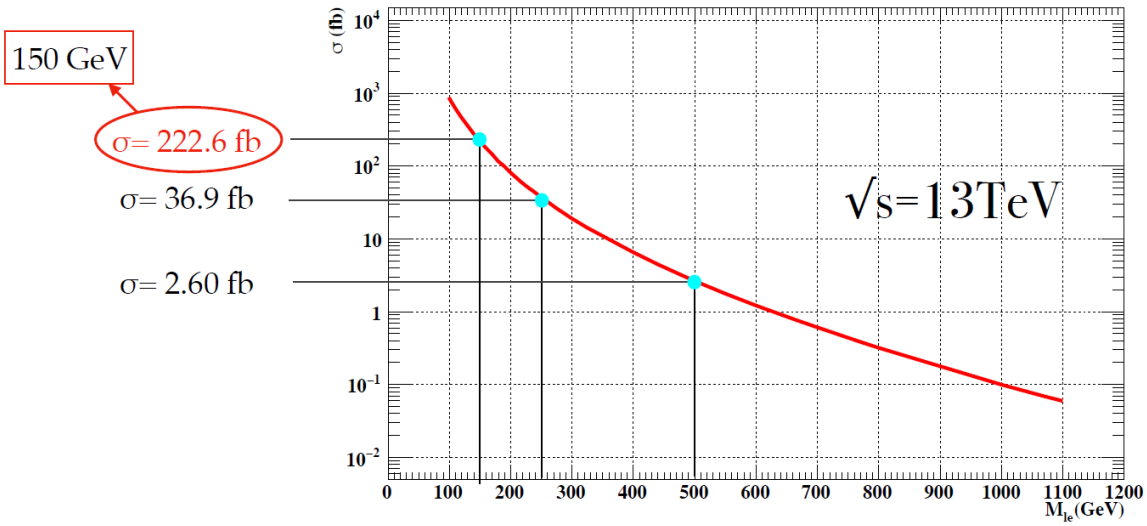

Figure 3.2. Pair production cross-section as a function of rest mass of isosinglet L_e produced by CompHEP [47].

The analysis uses CutLang [62] as its analysis framework and our team [63] contributes to its development. CutLang is a runtime interpreter of an analysis description language (ADL). In ADL, analyses are written in plain and easily readable text files. Objects, variables and event selection definitions are divided into blocks. ADL has a syntax that includes mathematical and logical operations, comparison and optimisation operators, four-vector algebra and other frequently used functions. The ADL file being used for this study is given in Appendix A. The software repository is on the internet [64].

Table 3.1. The cross-section, BR and number of signal events expected to occur in the ATLAS detector during Run2 for chosen rest masses of isosinglet L_e signal samples.

	150 GeV	**250 GeV**
$\sigma_{L_e\bar{L_e}}$ (pb)	2.226×10^{-1}	3.614×10^{-2}
$\sigma_{L_e\bar{L_e}}$ uncertainty (pb)	4.8×10^{-5}	6.9×10^{-6}
$BR(L_e \to Ze)$	0.289	0.275
$BR(L_e \to W\nu)$	0.673	0.563
Final State σ (pb)	3.93×10^{-3}	5.09×10^{-4}
Expected No of Events	547	70.7

Before starting the analysis, the initial focus of the team has been on improving the performance of the analysis framework that has been used during the study. Parallel processing option has been added to CutLang during this period. The improved performance of CutLang has been documented and included in a published paper [65] along with other developments in CutLang. In Figure 3.3, the number of events processed per second are shown when varying number of processors are utilized.

Due to the final state similarity, this study is a partner to another analysis: search for type-III seesaw heavy leptons in multi-lepton final states [66]. Thus we share the same data and background samples. All background MC samples are weighted to match data-taking conditions at the ATLAS detector. Two of these are luminosity and pile-up weights. Also, events are weighted to convert the number of generated MC events to the number of events that are expected to be observed at the ATLAS detector. These event weights are in the order of 1 for processes where generated MC events are comparable to the number of events to be observed. However, when a process is far from the final state of interest, they are represented by fewer generated events than what would actually be observed in the ATLAS detector. In this case, the weight can be in the order of 100. All background MC samples consist of many subsamples, and diboson has 18 of them.

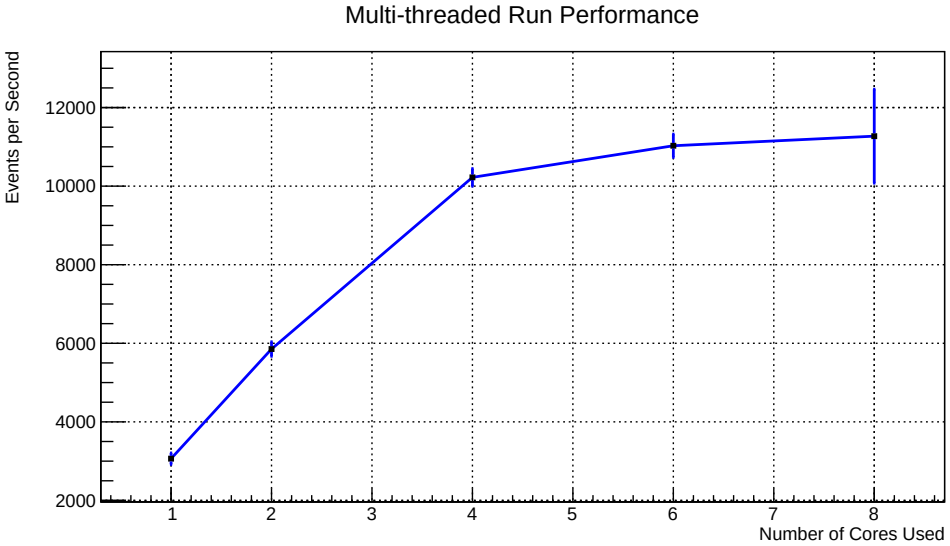

Figure 3.3. Processed events per second when 1, 2, 4, 6 or 8 threads are used [65]. Error bars are multiplied by 10 to make them visible. Test has been run on a computer that has 4 physical cores, each further divided into 2 logical cores, thus the runs that use more than 4 threads show minimal improvement.

A subsample of diboson process that is of interest to this study has a hadronically decaying W boson and a leptonically decaying Z boson. This subsample has a cross-section of 3.4329 pb, which is an order of magnitude greater than the total cross-section of L_e pair production as can be seen in Table 3.1. Thus, restricting the phase space with a selection process is crucial so that a prominent signal can be discerned from the background.

Before moving on with the analysis, it is essential to document the initial work done to make sure that our analysis framework produces results that are on par with the validated results obtained by our partner group. After learning how to process the samples, the surviving events after four event selections applied by our partner group in their analysis are reproduced in our analysis framework. The difference between the surviving events is within 0.5% for data and the dominant diboson background sample, as can be seen in Table 3.2.

The prefix "goodJET " and "goodleptons" given in the table are further restricted versions of the particle type by object definition criteria given in Section 3.2. Knowing that the framework is configured to obtain reliable results, we move on with our analysis detailed in the following sections.

Table 3.2. Comparison of surviving events based on the first four event selections applied in the partner groups cutflow. Here, "CutLang" refers to our results while "Athena" refers to results obtained by our partners using the Athena [67] framework.

	Data			**Diboson**		
	CutLang	**Athena**	**%diff.**	**CutLang**	**Athena**	**%diff.**
All	133752	133752	0.0%	31318.8	31318.8	0%
Size(goodJET) >= 2	55583	55583	0.0%	11776.7	11715.6	0.5%
Size(leptons) == 3	55583	55583	0.0%	11776.7	11715.6	0.5%
Size(goodleptons) == 3	14618	14618	0.0%	8800.3	8755.0	0.5%

3.1. Data and MC Samples

3.1.1. Data

The data used in this study was recorded by the ATLAS detector between the years 2015-2018 and has an integrated luminosity of $\mathcal{L} = 139\,\text{fb}^{-1}$. The luminosity uncertainty of the total data is 1.7%. Recorded data is grouped into good run lists (GRLs) if instantaneous luminosity is within certain limits at the time of recording and all the subdetectors are working well. The four periods we use in our study have integrated luminosity of $\mathcal{L}$ =3.2 fb^{-1} for 2015, $\mathcal{L}$ =33.0 fb^{-1} for 2016, $\mathcal{L}$ =43.8 fb^{-1} for 2017 and $\mathcal{L}$ =59.9 fb^{-1} for 2018.

3.1.2. Background MC Samples

Production parameters of all background MC samples are given in Table 3.3. The dominant backgrounds for the signal sought after are the diboson and rare top processes.

Table 3.3. Summary of simulated background event samples with the corresponding event generator, parton shower, cross-section normalisation, PDF set used for the matrix element and set of tuned parameters.

Physics process	**Event generator**	**PDF set**	**Cross-section normalization**	**Parton shower**	**Parton shower tune**
Z+jets					
$Z/\gamma^* \to e^+e^-/\mu^+\mu^-/\tau^+\tau^-$	Sherpa 2.2.1 [68]	NNPDF3.0NNLO [69]	NLO	PYTHIA 8.212	SHERPA default
Top physics					
$t\bar{t}$	Powheg-Box v2 [70]	NNPDF3.0NNLO	NNLO	PYTHIA 8.212	A14 [68]
Single t	Powheg-Box v2	NNPDF3.0NNLO	NNLO	PYTHIA 8.212	A14
Rare Top physics					
3t, 4t	MadGraph5_aMC@NLO	NNPDF2.3LO	LO	PYTHIA 8.212	A14
$t\bar{t}+W/Z$	MadGraph5_aMC@NLO	MEN30NLO	NNLO	PYTHIA 8.212	A14
Diboson					
ZZ, WZ	Sherpa 2.2.1 & 2.2.2	NNPDF3.0NNLO	NLO	PYTHIA 8.212	SHERPA default
Multiboson					
WWW, WWZ, WZZ, ZZZ	Sherpa 2.2.1 & 2.2.2	NNPDF3.0NNLO	NNLO	PYTHIA 8.212	SHERPA default

3.1.3. Signal MC Samples

Our group has generated the signal samples. Parton level generation was done by CompHEP [47] where the relevant Lagrangian was implemented by our group. Parton distribution function (PDF) CTEQ6 at leading order (LO) was used. The invariant mass reconstruction to control the generated events is given in Figures 3.4 and 3.5. Parton showering, fragmentation and hadronization has been done by PYTHIA8 [49]. Only two signal samples were initially generated for 150 GeV and 250 GeV rest mass of L_e. New signal samples have since been produced over the course of this study, which will be discussed in Chapter 4.

3.2. Baseline Event Selection and Object Definitions

The signitures for the used triggers are given in Table 3.4. Only dilepton triggers are considered for all regions to avoid trigger bias on fakes. As an example HLT_e17_lhloose_mu14 requires one electron above 17 GeV and one muon above 14 GeV.

Table 3.4. Summary of the trigger signitures.

	2015	**2016**	**2017+2018**
ee	HLT_2e12_lhloose_L12EM10VH	HLT_2e17_lhvloose_nod0	HLT_2e17_lhvloose_nod0_L12EM15VHI OR HLT_2e24_lhvloose_nod0
$e\mu$	HLT_e17_lhloose_mu14	HLT_e17_lhloose_nod0_mu14	HLT_e17_lhloose_nod0_mu14
$\mu\mu$	HLT_mu18_mu8noL1	HLT_mu22_mu8noL1	HLT_mu22_mu8noL1

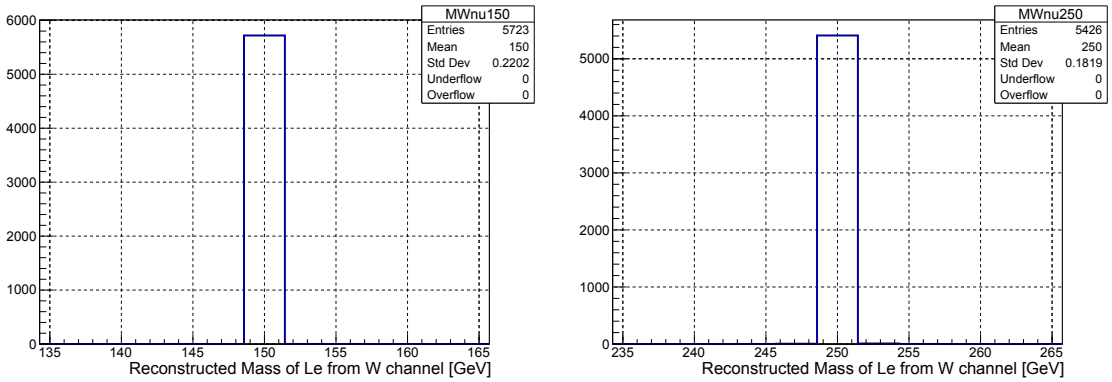

Figure 3.4. Invariant mass of reconstructed L_e from W channel at parton level generation for 150 (left) and 250 GeV (right) samples.

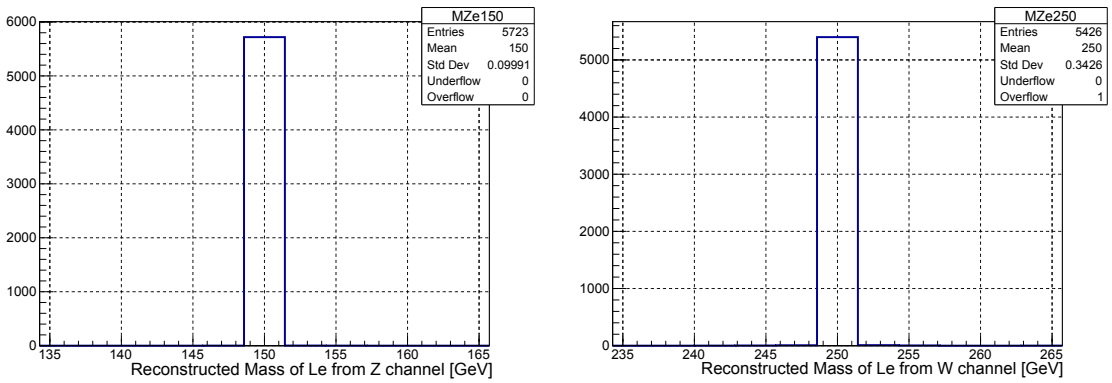

Figure 3.5. Invariant mass of reconstructed L_e from Z channel at parton level generation for 150 (left) and 250 GeV (right) samples.

The object definitions in our analysis are given below along with the ADL file listings:

- object goodELE : ELE : Electron definition used in the analysis
  - select AbsEta(ELE_) < 2.47 : Selects electrons that have $|\eta| < 2.47$
  - select AbsEta(ELE_)][1.37 1.52 : Selects electrons with $1.37 < |\eta| < 1.52$
  - select Pt(ELE_) > 10.0 : Selects electrons that have p_T >10 GeV
  - select LEPTIGHT(ELE_) == 0 : Selects electrons that satisfy Tight identification and FixedCutLoose isolation criteria

- object goodMUO : MUO : Muon definition used in the analysis
  - select AbsEta(MUO_) < 2.5 : Selects muons that have $|\eta| < 2.5$
  - select Pt(MUO_) > 10.0 : Selects muons that have p_T >10 GeV
  - select LEPTIGHT(MUO_) == 0 : Selects mons that satisfy Medium or HighPt if $p_T > 300$ GeV identification and FixedCutTightTrackOnly isolation

- object goodJET : JET : Jet definition used in the analysis
  - select AbsEta(JET_) < 2.5 : Selects jets that have $|\eta| < 2.5$
  - select Pt(JET_) > 20.0 : Selects jets that have p_T >20 GeV

Additionally, there is a requirement of having at least two leptons with transverse momenta greater than 40 GeV. This is achieved in the preselection phase of analysis.

3.3. Analysis Regions and Determination of Event Selections

This chapter elaborates the method used to determine the event selection parameters, and then the selections applied to pre-selection and signal regions are given with generated histograms.

3.3.1. Determination Method of Event Selection Criteria

In order to determine the event selection steps, a method to maximize significance is implemented. An additional plot where the contribution of each bin to the signal significance is drawn as can be seen in Figure 3.6. The values are calculated by the ratio of $\mathcal{S}$ when the number of events in the bins of original histogram are included in the calculation to the case that they are excluded. Positive values mean that the $\mathcal{S}$ is lower when the bin contents are excluded from the significance calculation. Then, a normalized histogram is plotted using these values to get a visual input as to where the event selection should be applied. Including a point where the marker is below zero indicates a drop in the signal significance, so an event selection that keeps the positively valued bins and discards the rest is applied. The event selections presented in the coming sections are chosen using this method.

The significance $\mathcal{S}$ is calculated as

$$\mathcal{S} = \sqrt{2[(s+b)\log(1+s/b) - s]} \tag{3.2}$$

where, s and b are the numbers of expected signal and background events in the whole histogram. For a discovery, $\mathcal{S} > 5$ is the accepted level [71].

3.3.2. Pre-Selection

The pre-selections are used to determine the event selections that will be used in each analysis region which are implemented as 12 steps in CutLang as listed below and figures obtained after that step are given in paranthesis. While most of these steps are self-explanatory, it is worth describing the $\sim=$ operator. This operator is not an event selection but acts as a tagging mechanism. It tries to minimize the difference between the function on the left and the value given on the right by χ^2 minimization [65]. An example of this is the $Zfunc$ function of the 6^{th} step.

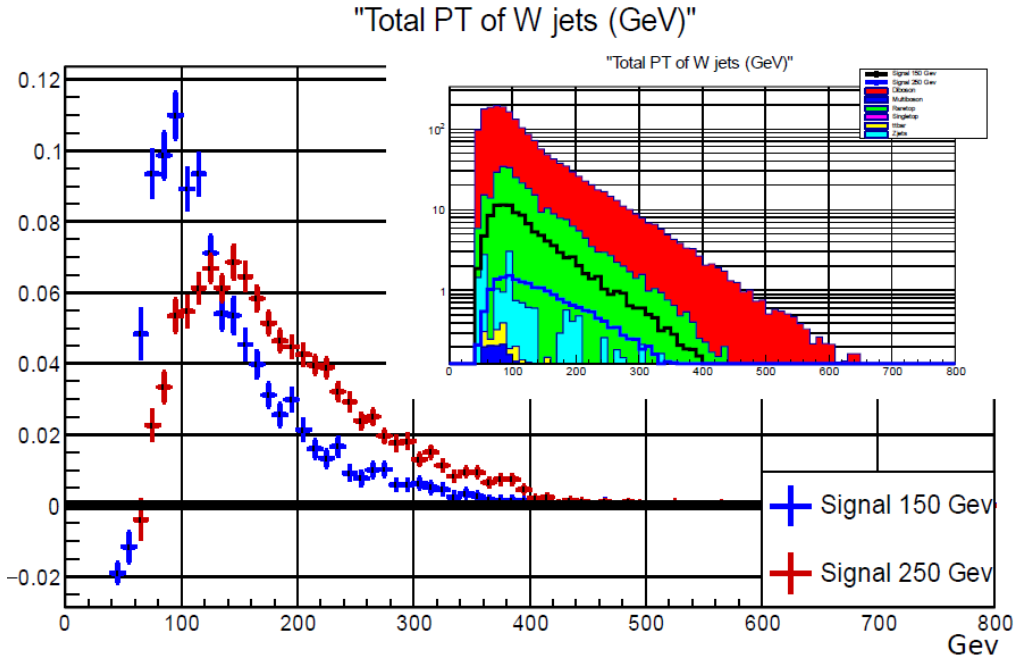

Figure 3.6. Histogram of the total p_T of the jets tagged as W candidates are given in the inset, and the main plot depicts the significance contribution graph. In this example, it is seen that excluding total $p_T < 60$ GeV increases significance for both 150 and 250 GeV signal samples.

This function tries to find and label the best Z candidates out of all available leptons by choosing 2 same flavor leptons l_{Z1} and l_{Z2} with the opposite charge that has a minimum difference with the rest mass of Z boson (∼91 GeV) when combined. CutLang also gives its user the ability to define objects with desired properties. As an example, the electrons and muons with the required properties given in Section 3.2 are named as "goodleptons" and the analysis is based on them. The pre-selection steps are:

1) Size(goodleptons) == 3 : Selects events with 3 light leptons, electron and muon (Figure 3.7)

2) pt(goodleptons_0) > 40.0 : Selects events where lepton with largest transverse momentum has p_T larger than 40 GeV

3) pt(goodleptons_1) > 40.0 : Selects events where lepton with second largest transverse momentum has p_T larger than 40 GeV

4) Size(goodJET) >= 2 : Selects events with at least 2 jets

5) Size(goodELE) == 1 OR Size(goodELE) == 3 : Selects events with either 1 or 3 electrons

6) Zfunc ~= 0.0 : As stated above. The remaining lepton is labelled as l_3

7) pdgidDiff == 0 : Selects events where Z candidates l_{Z1} and l_{Z2} have the same flavor

8) q(Zreco) == 0 : Selects events where Z candidates l_{Z1} and l_{Z2} have opposite charge. Here, the "Zreco" is the object reconstructed by said leptons (Figure 3.8)

9) m(Zreco) [] 85 95 : Selects events where combined invariant mass of l_{Z1} and l_{Z2} is in the interval of 85 to 95 GeV

10) abs(PDGID(l3)) == 11 : Selects events where l_3 is an electron

11) m(Wreco) ~= 80 : Finds the best W boson candidates and labels them as j_1 and j_2 by finding a pair of jets that have a combined invariant mass as close to W boson mass (~80 GeV) as possible (Figure 3.8)

12) m(Wreco) [] 50 110 : Selects events where combined invariant mass of j_1 and j_2 is in the interval of 50 to 110 GeV (Figures 3.9 and 3.10)

3.3.3. Signal Region

In this region, the event selections are applied to increase the signal to background event ratio, and thus $\mathcal{S}$ is maximized. An explicit description of each signal region event selection is given below:

1) METsig > 1.0 : Selects events with $\mathcal{S}(E_T^{miss.})$ larger than 1

2) abs (goodLEPC , Zreco dR) < 3.1 : Selects events with the angular distance between the reconstructed Z boson, and the remaining lepton is less than 3.1

3) { goodJETA }Pt + { goodJETB }Pt > 60 : Selects events where the scalar sum of the transverse momenta of W candidate jets is more than 60 GeV

4) MET + { goodJETA }Pt + { goodJETB }Pt > 120 : Selects events where the scalar sum of total transverse momenta of W candidate jets and $E_T^{miss.}$ is more than 120 GeV (Figures 3.11 and 3.12)

5) { LeW , LeZ} dR [] 2.6 4.1 : Selects events where the angular distance between two reconstructed Le from W and Z boson channels is in the interval of 2.6 to 4.1

6) pt(LeW) > 40.0 : Selects events with transverse momenta of Le_W larger than 40 GeV

7) pt(LeZ) > 40.0 : Selects events with transverse momenta of Le_Z larger than 40 GeV

8) abs(m(LeZ) -m(LeW)) < 160 : Selects events where the recombined mass difference between Le_W and Le_Z is less than 160 GeV, used to eliminate processes that are highly unlikely to come from the decay channel studied

9) pt(l3) > 40.0 : Selects events where transverse momentum of the lepton that is not a daugther of the Z candidate to be more than 40 GeV (Figures 3.13 to 3.17)

The dominant background is from diboson process, constituting about 83.4% of all background after the final event selection of the signal region is applied. Rare top processes are the second dominant process, and they account for about 99.8% of the background together with the diboson processes. The event yields after each event selection of the analyis is given in Table 3.5.

The histograms obtained during the study can be seen in the following figures. Up to the end of pre-selection criteria, histograms include the data and ratio of the data to the sum of all background processes is plotted below in each Figure from 3.7 to 3.10. The Figures 3.11 to 3.17 do not show the data since the analysis is done in a blinded state so that whether the signal is present is not shown until data to MC sample ratio agreement is proven. Additional results are given in the Appendix B.

Table 3.5. Event yields of signal and background samples in the signal region.

	Signal 150GeV	**Signal 250GeV**	**Diboson**	**Rare top**	**Data**
All Events	546.6±2.6	73.1±0.3	(3.132±0.042)×10^4	(2.170±0.004)×10^3	(1.338±0.004)×10^5
Pre-Selection					
1) Size(goodleptons) == 3	299.5±1.9	41.9±0.2	(2.370±0.032)×10^4	(1.664±0.003)×10^3	(3.856±0.020)×10^4
2) pt(goodleptons_0) > 40.0	296.4±1.9	41.9±0.2	(2.370±0.032)×10^4	(1.664±0.003)×10^3	(3.856±0.020)×10^4
3) pt(goodleptons_1) > 40.0	226.0±1.6	40.3±0.2	(2.370±0.032)×10^4	(1.664±0.003)×10^3	(3.856±0.020)×10^4
4) Size(goodJET) >= 2	159.2±1.4	30.6±0.2	(8.760±0.013)×10^3	(1.530±0.003)×10^3	(1.455±0.012)×10^4
5) Size(goodELE) == 1 OR Size(goodELE) == 3	159.0±1.4	30.6±0.2	(4.040±0.008)×10^3	712.2±2.1	7550±87
6) Zfunc ∼= 0.0	159.0±1.4	30.6±0.2	(4.040±0.008)×10^3	712.2±2.1	7550±87
7) pdgidDiff == 0	159.0±1.4	30.6±0.2	(4.036±0.008)×10^3	679.0±2.0	7329±86
8) q(Zreco) == 0	158.3±1.4	30.4±0.2	(4.024±0.008)×10^3	659.4±2.0	7228±85
9) m(Zreco) [] 85 95	142.9±1.3	27.0±0.2	(2.831±0.007)×10^3	377.6±1.5	4170±64
10) abs(PDGID(l3)) == 11	142.9±1.3	27.0±0.2	(2.831±0.007)×10^3	377.6±1.5	4170±64
11) m(Wreco) ∼= 80	142.9±1.3	27.0±0.2	(2.831±0.007)×10^3	377.6±1.5	4170±64
12) m(Wreco) [] 50 110	114.9±1.2	21.8±0.2	(1.573±0.005)×10^3	293.5±1.3	2413±49
Signal Region					
1) METsig > 1.0	107.2±1.1	21.3±0.2	(1.356±0.004)×10^3	266.8±1.3	
2) abs (goodLEPC , Zreco dR) < 3.1	103.5±1.1	19.4±0.2	(1.063±0.003)×10^3	219.5±1.1	
3) goodJETA t U goodJETB t > 60	97.5±1.1	18.7±0.2	907.7±2.9	207.1±1.1	
4) MET U goodJETA t U goodJETB t > 120	91.0±1.0	18.6±0.2	774.3±2.6	194.1±1.1	
5) LeW , LeZ dR [] 2.6 4.1	80.2±1.0	1.62±0.1	537.7±2.3	117.2±0.8	
6) pt(LeW) > 40.0	77.5±1.0	1.60±0.1	512.0±2.2	111.7±0.8	
7) pt(LeZ) > 40.0	76.7±1.0	1.59±0.1	502.4±2.2	108.9±0.8	
8) abs(m(LeZ) - m(LeW)) < 160	72.0±0.9	1.48±0.1	406.3±2.0	87.9±0.7	
9) pt(l3) > 40.0	59.7±0.8	1.44±0.1	313.2±1.7	61.9±0.6	

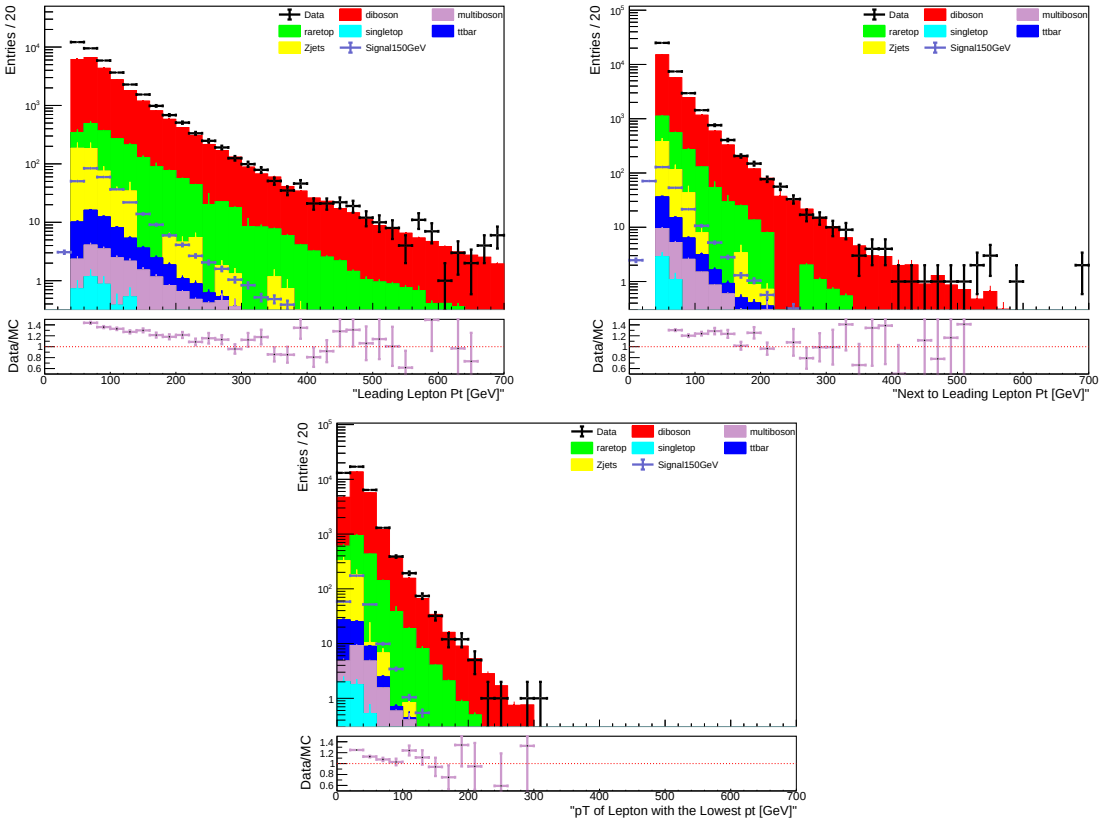

Figure 3.7. p_T distributions of the leptons after the 1^{st} pre-selection criteria.

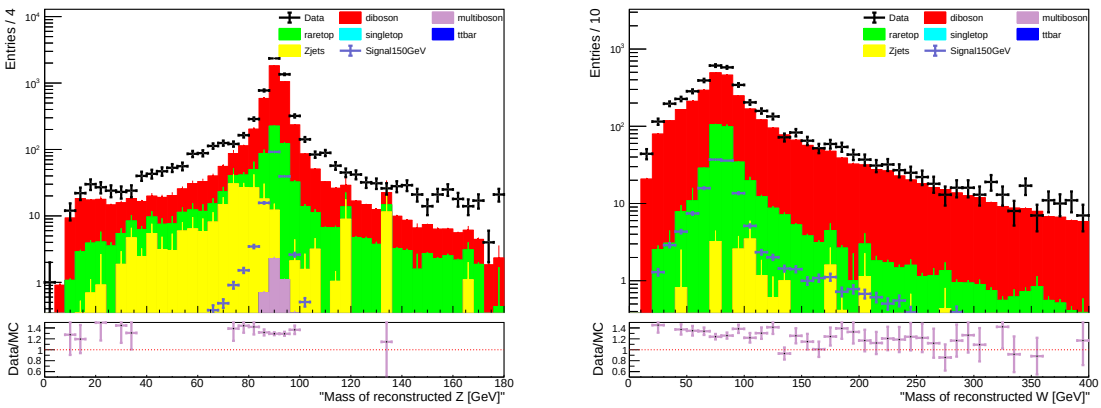

Figure 3.8. Masses of reconstructed Z and W before their mass window event selection which are 9^{th} and 12^{th} pre-selection criteria respectively.

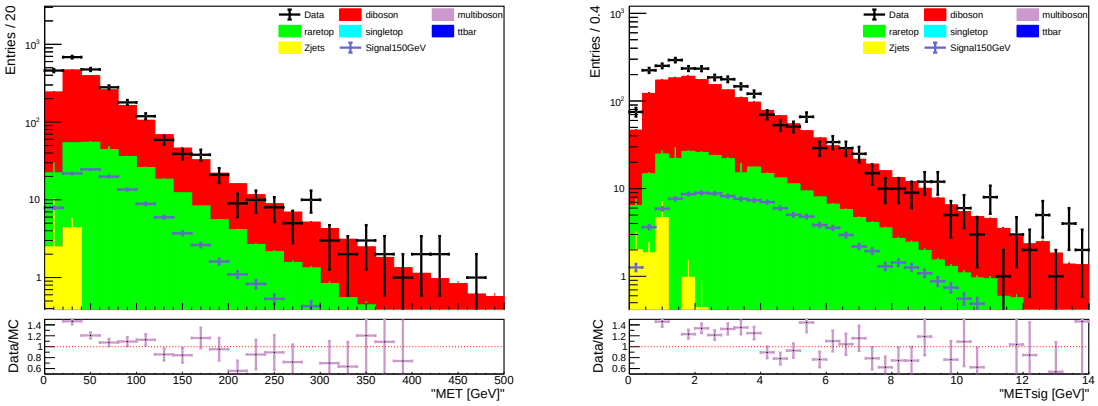

Figure 3.9. $E_T^{miss.}$ and $\mathcal{S}(E_T^{miss.})$ distributions after the pre-selection criteria.

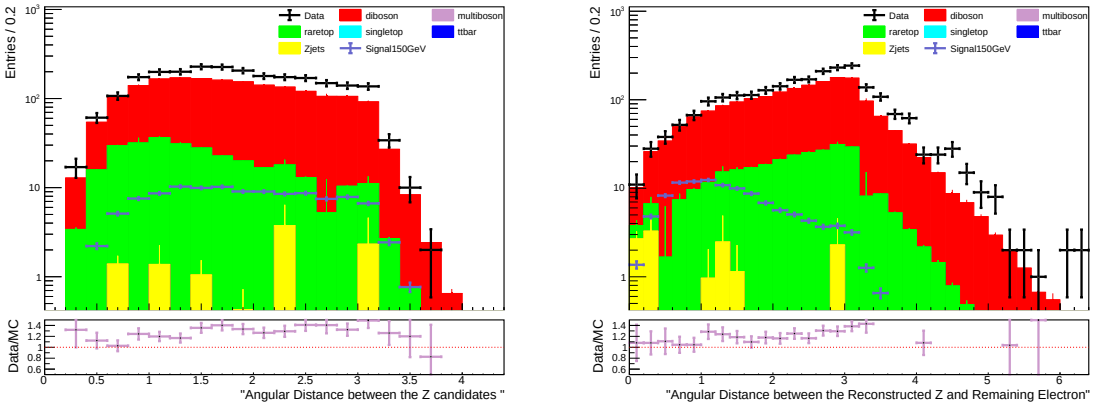

Figure 3.10. Angular distance distributions between Z candidates and between reconstructed Z and electron of $L_e \to Ze$ decay after the pre-selection criteria.

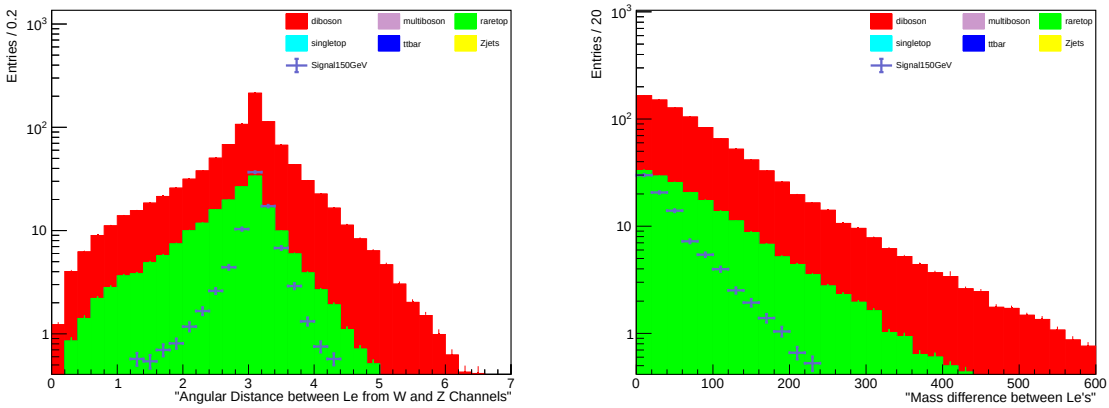

Figure 3.11. The mass and angular distance difference between reconstructed L_e's after the 4^{th} signal region selection.

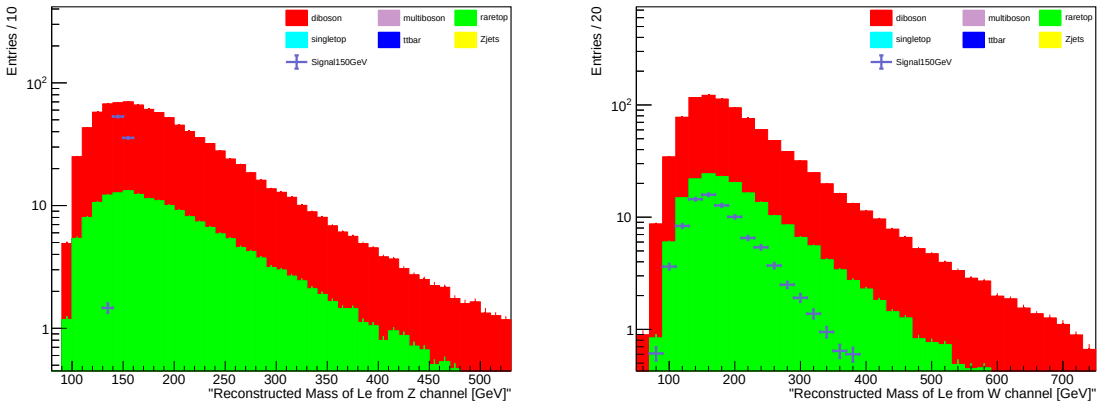

Figure 3.12. Invariant masses of reconstructed L_e's after the 4^{th} signal region selection.

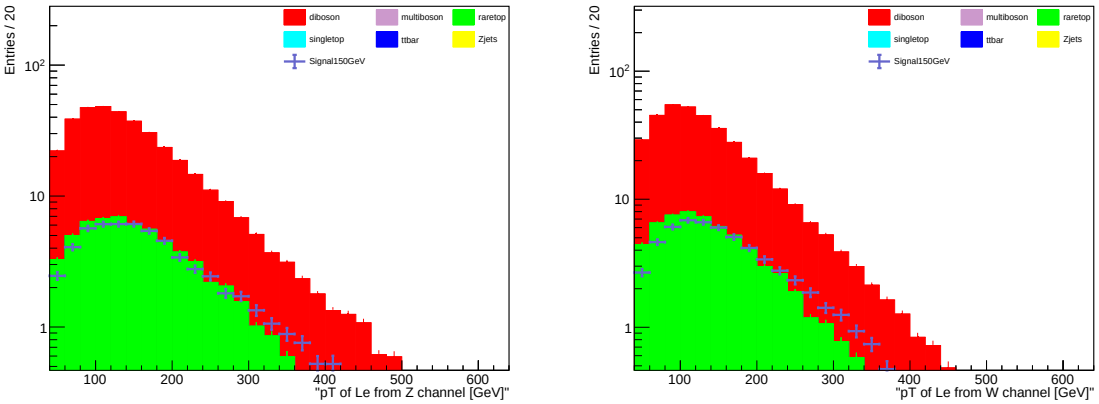

Figure 3.13. p_T of reconstructed L_e's after the final signal region selection.

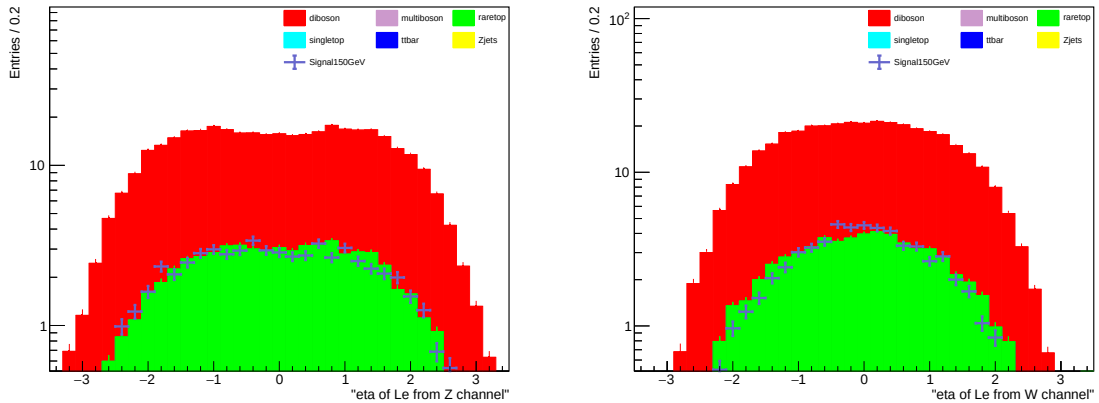

Figure 3.14. η of reconstructed L_e's after the final signal region selection.

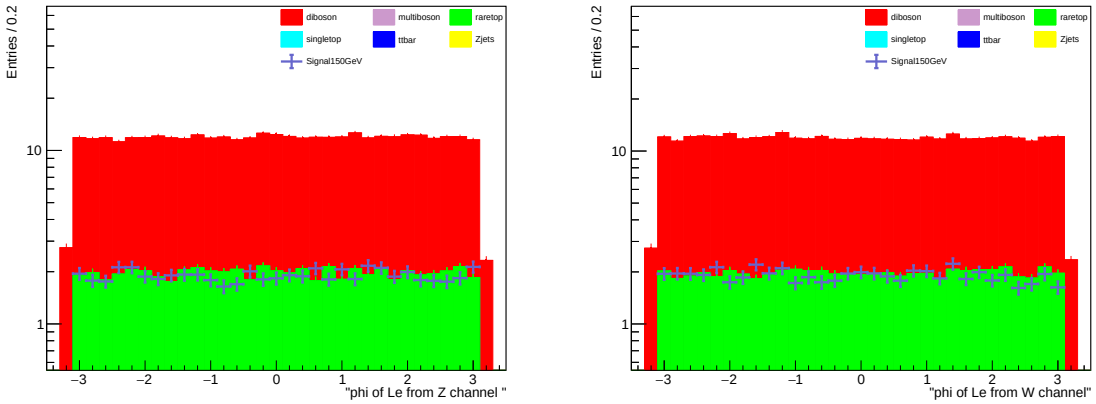

Figure 3.15. ϕ of reconstructed L_e's after the final signal region selection.

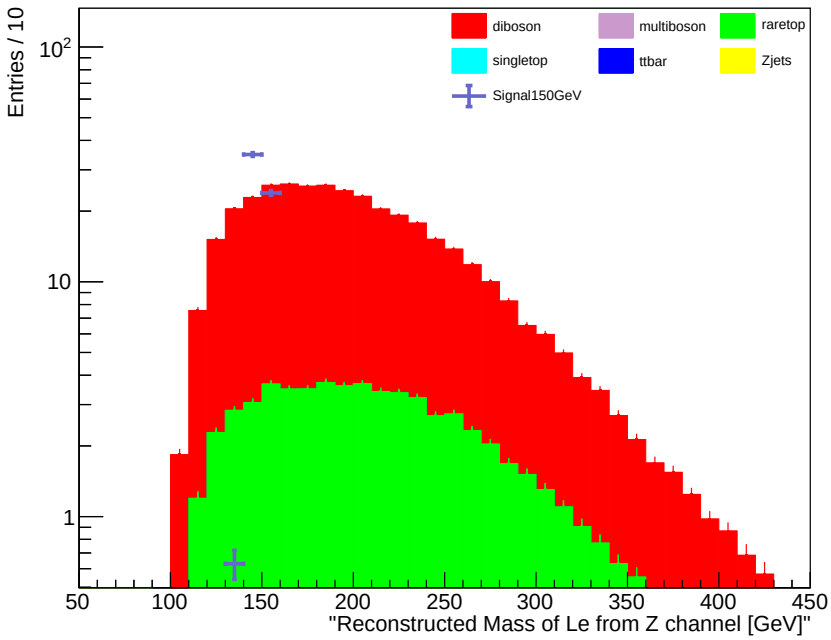

Figure 3.16. Invariant mass of reconstructed L_e from Z channel after the final signal region selection.

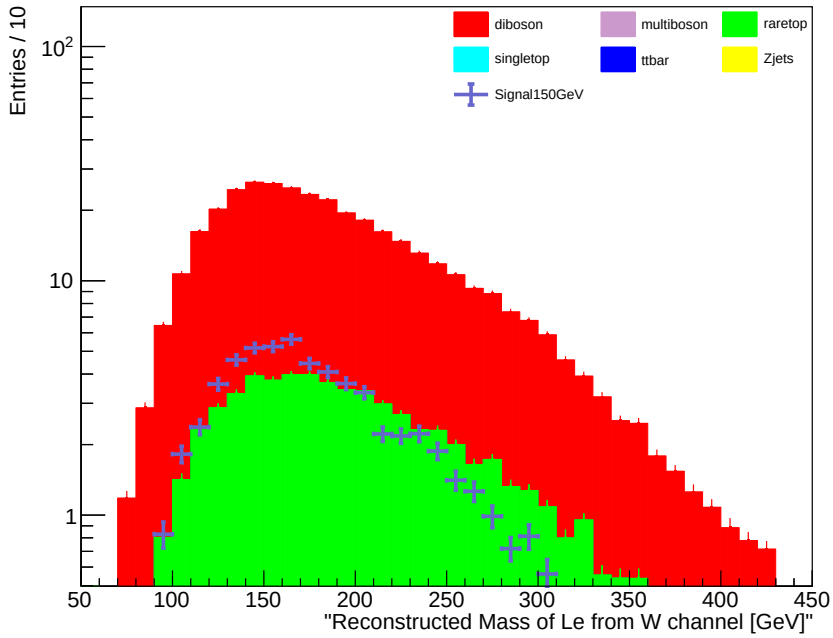

Figure 3.17. Invariant mass of reconstructed L_e from W channel after the final signal region selection.

4. RESULTS

The signal significance after the signal region event selection is 3.0 and 0.74 for 150 and 250 GeV signal samples, respectively. After the completion of signal region analysis, limit plots using TRExFitter [72] tool has been created, which can be seen in Figure 4.1. TRExFitter is a widely used framework to obtain profile likelihood fits. The expected limit does not seem to fall below 250 GeV and the highest mass signal sample we have during the first round of the analysis is 250 GeV, so a pseudo result is created by reweighting the results of the signal sample with 250 GeV. This is achieved by changing the branching ratio and cross-section of 250 GeV sample to the branching ratio and cross-section of 350 GeV L_e.

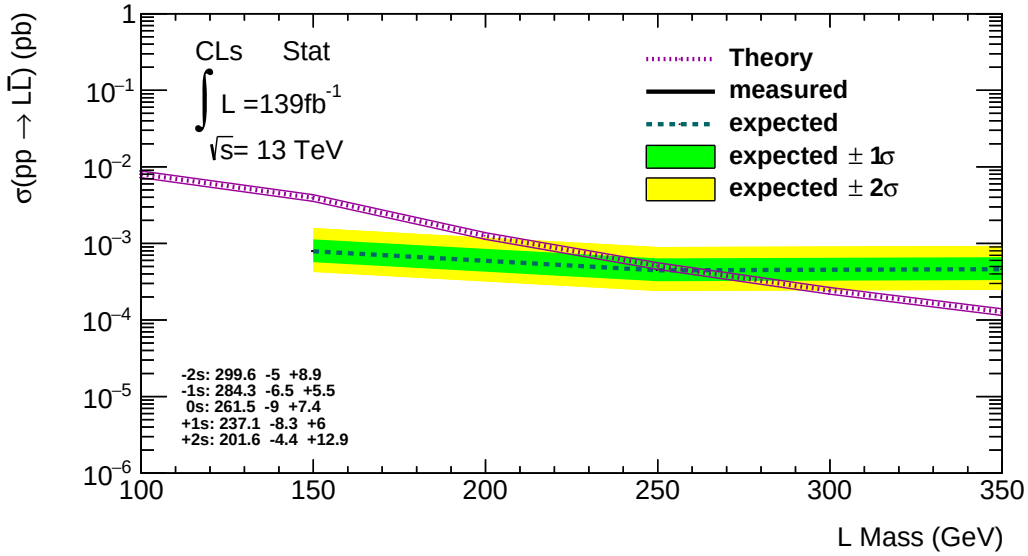

Figure 4.1. Expected 95% CLs exclusion limit with one and two standard deviation bands.

Only statistical uncertainty in the generation of exclusion limit plot is considered. By adding a 20% percent uncertainty in addition to the statistical uncertainty, the effects of systematics are simulated. The resulting exclusion limit plot is given in Figure 4.2.

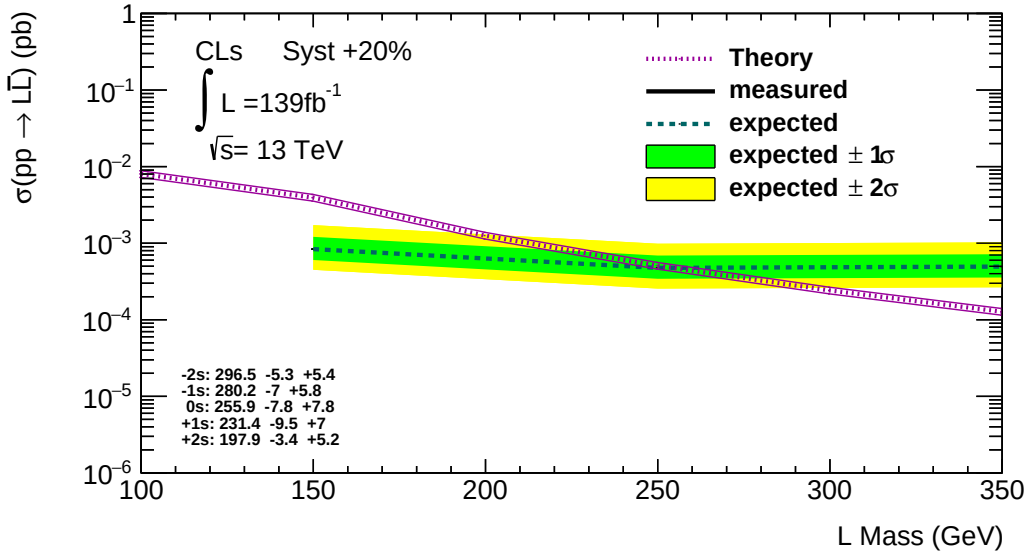

Figure 4.2. Expected 95% CLs exclusion limit with one and two standard deviation bands when an uncertainty of 20% is added to MC samples to account for missing systematic uncertainties.

These results have been shared with the ATLAS Exotics subgroup LPX. Since the analysis shows promise to move the previously set limit of 100.8 GeV [73] to about 250 GeV, the collaboration has approved the production of new signal samples with additional mass points of 200 and 300 GeV. The new samples are produced with the same PDF as background MC samples, and the search switched from isosinglet L_e to isodoublet L_e which has a higher cross-section $\sigma_{L_e\bar{L_e}}$ as shown in Table 4.1 and Figure 4.7. After generating events with CompHEP-4.5.2 [74] in LesHouches event (LHE) format, the hadronization and detector simulations are done by PYTHIA8.1 [49] and Delphes [50], respectively. Delphes is chosen to check quickly with fast simulation option it provides. The invariant mass reconstructions of L_e for each sample mass point on both W and Z channels have been checked and they are given in Figures 4.3 to 4.6. In the time of writing this thesis, the event production has concluded successfully.

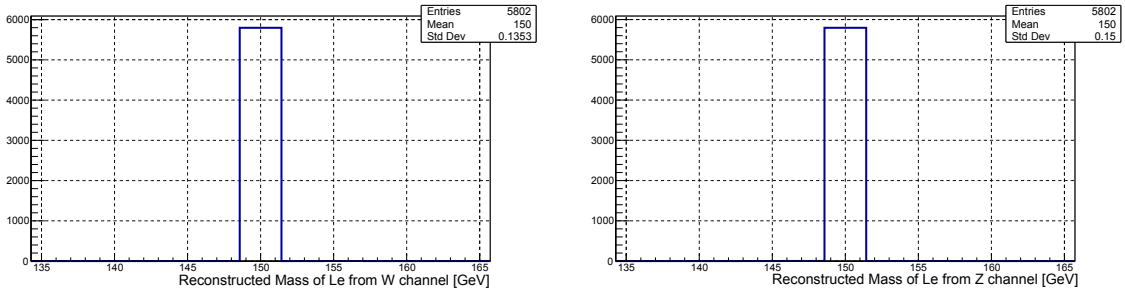

Figure 4.3. Invariant masses of reconstructed L_e's from W (left) and Z (right) channels at parton level generation for 150 GeV sample.

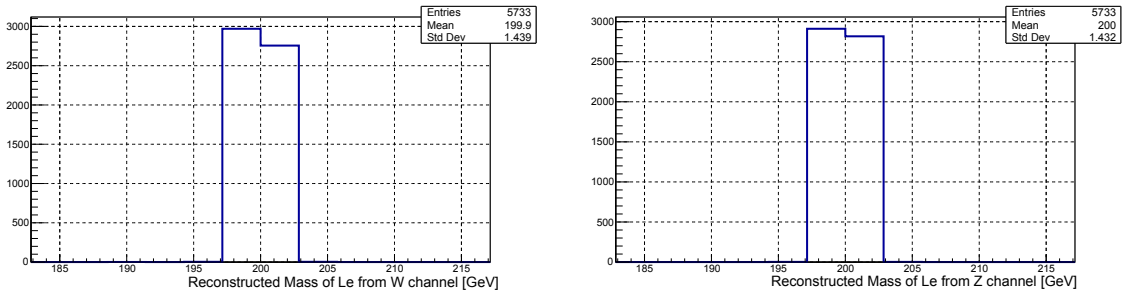

Figure 4.4. Invariant masses of reconstructed L_e's from W (left) and Z (right) channels at parton level generation for 200 GeV sample.

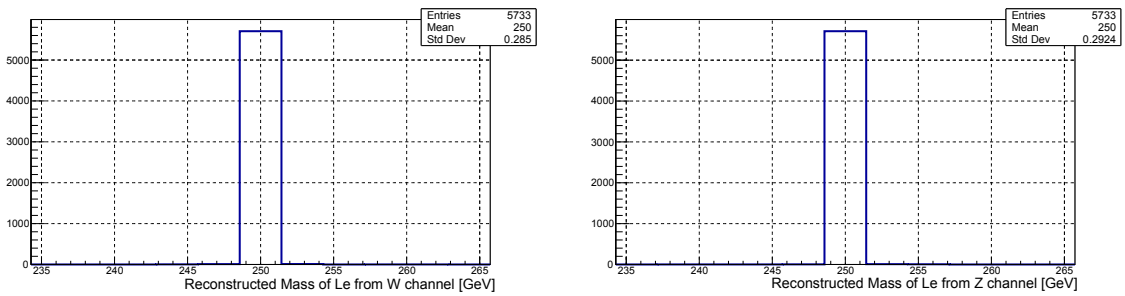

Figure 4.5. Invariant masses of reconstructed L_e's from W (left) and Z (right) channels at parton level generation for 250 GeV sample.

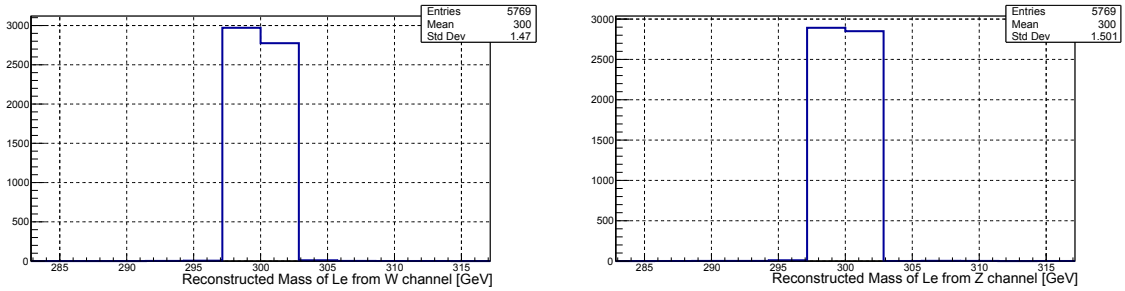

Figure 4.6. Invariant masses of reconstructed L_e's from W (left) and Z (right) channels at parton level generation for 300 GeV sample.

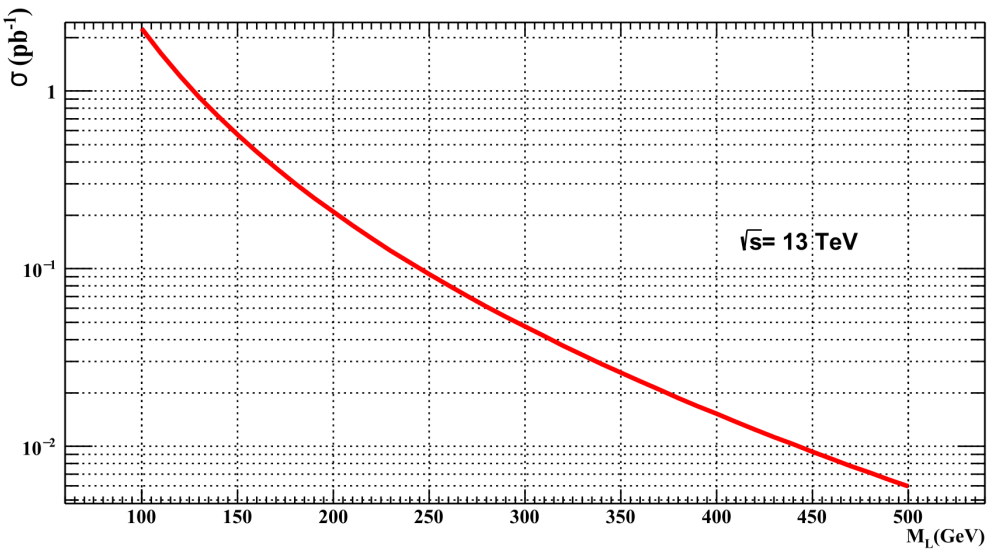

Figure 4.7. Pair production of cross-section as a function of rest mass of isosdoublet L_e produced by CompHEP.

Table 4.1. The cross-section, BR and number of signal events expected to occur in the ATLAS detector during Run2 for chosen rest masses of isodoublet L_e signal samples.

	150 GeV	**200 GeV**	**250 GeV**	**300 GeV**
$\sigma_{L_e\bar{L_e}}$ (pb)	5.687×10^{-1}	2.089×10^{-1}	9.345×10^{-2}	4.729×10^{-2}
$\sigma_{L_e\bar{L_e}}$ error (pb)	1.1×10^{-4}	3.7×10^{-5}	1.6×10^{-5}	7.7×10^{-6}
$BR(L_e \to Ze)$	0.289	0.284	0.275	0.269
$BR(L_e \to W\nu)$	0.673	0.597	0.563	0.544
Final State σ (pb)	1.00×10^{-2}	3.23×10^{-3}	1.32×10^{-3}	6.28×10^{-4}
Expected No of Events	1397	449	183	87.3

4.1. Future Plans

The signal region will be rechecked if the event selections are as efficient as they can be. After that, the control regions for diboson and rare top MC samples will be defined, and the analysis will be repeated with systematic uncertainties. Broadening our search to include other decay channels of L_e will be the next step in our search.

5. CONCLUSION

An account of the search for pair produced heavy iso-singlet leptons predicted by Grand Unified Theory based on group E_6 has been given in this work. The search has been conducted through discovery channel $pp \rightarrow L_e\bar{L}_e \rightarrow ZeW\nu_e \rightarrow 3l\,2j\,E_T^{miss}$ in ATLAS Run2 data which has an integrated luminosity of $\mathcal{L} = 139fb^{-1}$. CutLang was the analysis framework used during this study which brings to focus the physics analysis design rather than programming technicalities. A signal region is constructed by choosing event selection criteria that maximize the signal significance $\mathcal{S}$. The signal significances are calculated to be 3.0 using the 150 GeV signal sample and 0.74 using the 250 GeV signal sample. After the final event selection of the signal region, the event yields are used to produce an exclusion limit plot where the lower mass limit is found to be about 250 GeV. The previously set lower mass limit of 100.8 GeV was obtained by using L3 detector data of Large Electron-Positron Collider (LEP) in 2001. In conclusion, this study shows that a much higher lower mass limit is attainable by using ATLAS Run2 data.

With these encouraging results, the next goal of our team will be the production of new signal samples with additional mass points and repeating the search with these samples, including the systematics.

REFERENCES

1. CMS Collaboration, "Observation of a New Boson at a Mass of 125 GeV with the CMS Experiment at the LHC", *Physics Letters B*, Vol. 716, No. 1, pp. 30–61, 2012.

2. ATLAS Collaboration, "Observation of a New Particle in the Search for the Standard Model Higgs Boson with the ATLAS Detector at the LHC", *Physics Letters B*, Vol. 716, No. 1, pp. 1–29, 2012.

3. Higgs, P. W., "Broken Symmetries and the Masses of Gauge Bosons", *Physics Review Letters*, Vol. 13, pp. 508–509, Oct 1964.

4. Englert, F. and R. Brout, "Broken Symmetry and the Mass of Gauge Vector Mesons", *Physics Review Letters*, Vol. 13, pp. 321–323, Aug 1964.

5. Wikimedia Commons, *Standard Model of Elementary Particles*, 2021, `https://commons.wikimedia.org/wiki/File:Standard\_Model\_of\_Elementary\_Particles.svg`, accessed in June 2021.

6. Zyla, P. *et al.*, "Review of Particle Physics", *Progress of Theoretical and Experimental Physics*, Vol. 2020, No. 8, p. 083C01, 2020.

7. Glashow, S. L., "Partial Symmetries of Weak Interactions", *Nuclear Physics*, Vol. 22, pp. 579–588, 1961.

8. Weinberg, S., "A Model of Leptons", *Physics Review Letters*, Vol. 19, pp. 1264–1266, 1967.

9. Salam, A., "Weak and Electromagnetic Interactions", *Conference Proceedings*, Vol. C680519, pp. 367–377, 1968.

10. The Nobel Foundation, *The Nobel Prize in Physics 1979*, 2021, `https://www.`

nobelprize.org/prizes/physics/1979/summary/, accessed in June 2021.

11. Mannel, T., "Theory and Phenomenology of CP Violation", *Nuclear Physics B - Proceedings Supplements*, Vol. 167, pp. 170–174, 2007, proceedings of the 7th International Conference on Hyperons, Charm and Beauty Hadrons.

12. Adler, R. J., B. Casey and O. C. Jacob, "Vacuum Catastrophe: An Elementary Exposition of the Cosmological Constant Problem", *American Journal of Physics*, Vol. 63, No. 7, pp. 620–626, 1995.

13. Planck Collaboration, "Planck 2015 results - I. Overview of Products and Scientific Results", *Astronomy & Astrophysics*, Vol. 594, p. A1, 2016.

14. Particle Data Group, "Review of Particle Physics", *Progress of Theoretical and Experimental Physics*, Vol. 2020, No. 8, p. 32, 2020, 083C01.

15. Georgi, H. and S. L. Glashow, "Unity of All Elementary-Particle Forces", *Physics Review Letters*, Vol. 32, pp. 438–441, Feb 1974.

16. Gursey, F., P. Ramond and P. Sikivie, "A Universal Gauge Theory Model Based on E6", *Physics Letters*, Vol. 60B, pp. 177–180, 1976.

17. Osman Acar, A., O. E. Delialioglu and S. Sultansoy, "A Search for the First Generation Charged Vector-like Leptons at Future Colliders", *arXiv e-prints*, p. arXiv:2103.08222, Mar. 2021.

18. Aguilar-Saavedra, J., "Heavy Lepton Pair Production at LHC: Model Discrimination with Multi-lepton Signals", *Nuclear Physics B*, Vol. 828, No. 1, pp. 289–316, 2010.

19. CERN, *CERN Annual Report 2020*, Tech. rep., CERN, Geneva, 2021.

20. De Melis, C., *The CERN Accelerator Complex. Complexe des Accélérateurs du*

CERN, Jan 2016, https://cds.cern.ch/record/2119882, accessed in June 2021.

21. CERN, "LHC Guide", Geneva, Mar 2017.

22. ATLAS Collaboration, *Luminosity Public Results Run2*, https://atlas.web.cern.ch/Atlas/GROUPS/DATAPREPARATION/PublicPlots/2018/DataSummary/figs/intlumivstimeRun2DQall.png, accessed in June 2021.

23. ATLAS Collaboration, *Luminosity Public Results Run2*, https://atlas.web.cern.ch/Atlas/GROUPS/DATAPREPARATION/PublicPlots/2018/DataSummary/figs/mu_2015_2018.png, accessed in June 2021.

24. ATLAS Collaboration, "The ATLAS Experiment at the CERN Large Hadron Collider", *Journal of Instrumentation*, Vol. 3, No. 08, pp. S08003–S08003, aug 2008.

25. Pequenao, J., *Computer Generated Image of the Whole ATLAS Detector*, Mar 2008, https://cds.cern.ch/record/1095924, accessed in June 2021.

26. Pequenao, J. and P. Schaffner, *How ATLAS detects particles: diagram of particle paths in the detector*, Jan 2013, https://cds.cern.ch/record/1505342, accessed in June 2021.

27. Schott, M. and M. Dunford, *Illustration of the ATLAS and CMS Coordinate System.*, May 2014, http://cds.cern.ch/record/1699952/files/Figures_T_Coordinate.png, accessed in June 2021.

28. ATLAS Collaboration, *ATLAS Inner Detector: Technical Design Report. Vol. 1*, CERN, Geneva, 1997.

29. ATLAS Collaboration, *ATLAS Inner Detector: Technical Design Report. Vol. 2*, CERN, Geneva, 1997.

30. Ferrère, D., "The Upgrade of the ATLAS Inner Detector", *Nuclear Instruments*

and Methods in Physics Research Section A: Accelerators, Spectrometers, Detectors and Associated Equipment, Vol. 718, pp. 30–38, 2013, proceedings of the 12th Pisa Meeting on Advanced Detectors.

31. Pequenao, J., *Computer generated image of the ATLAS inner detector*, Mar 2008, `https://cds.cern.ch/record/1095926`, accessed in June 2021.

32. Capeans, M. *et al.*, *ATLAS Insertable B-Layer Technical Design Report*, Tech. rep., CERN, 2010.

33. Pernegger, H., *The Pixel Detector of the ATLAS Experiment for LHC Run-2*, Tech. rep., CERN, Geneva, Feb 2015.

34. ATLAS Collaboration, "Operation and Performance of the ATLAS Semiconductor Tracker", *Journal of Instrumentation*, Vol. 9, No. 08, pp. P08009–P08009, aug 2014.

35. ATLAS TRT Collaboration, "The ATLAS Transition Radiation Tracker (TRT) proportional drift tube: design and performance", *Journal of Instrumentation*, Vol. 3, No. 02, pp. P02013–P02013, feb 2008.

36. Pequenao, J., *Computer Generated Image of the ATLAS Calorimeter*, Mar 2008, `http://cds.cern.ch/record/1095927`, accessed in June 2021.

37. ATLAS Collaboration, *ATLAS Liquid-Argon Calorimeter: Technical Design Report*, Technical design report. ATLAS, CERN, Geneva, 1996.

38. ATLAS Collaboration, "The ATLAS Experiment at the CERN Large Hadron Collider", *Journal of Instrumentation*, Vol. 3, p. S08003. 437 p, 2008.

39. ATLAS Collaboration, *ATLAS Tile Calorimeter: Technical Design Report*, Technical design report. ATLAS, CERN, Geneva, 1996.

40. Palestini, S., "The Muon Spectrometer of the ATLAS Experiment", *Nuclear Physics B - Proceedings Supplements*, Vol. 125, pp. 337–345, 2003.

41. ATLAS Collaboration, "Muon Reconstruction Performance of the ATLAS Detector in Proton–Proton Collision Data at $\sqrt{s}$ =13 TeV", *The European Physical Journal C*, Vol. 76, No. 5, p. 292, 2016.

42. Bauer, F. *et al.*, "Construction and Test of MDT Chambers for the ATLAS Muon Spectrometer", *Nuclear Instruments and Methods in Physics Research Section A: Accelerators, Spectrometers, Detectors and Associated Equipment*, Vol. 461, pp. 17–20, 2001.

43. Argyropoulos, T. *et al.*, "Cathode Strip Chambers in ATLAS: Installation, Commissioning and in Situ Performance", *IEEE Transactions on Nuclear Science*, Vol. 56, pp. 1568–1574, 2009.

44. Aielli, G. *et al.*, "The RPC First Level Muon Trigger in the Barrel of the ATLAS Experiment", *Nuclear Physics B - Proceedings Supplements*, Vol. 158, pp. 11–15, 2006.

45. Pequenao, J., *Computer Generated Image of the ATLAS Muons Subsystem*, Mar 2008, `https://cds.cern.ch/record/1095929`, accessed in June 2021.

46. ATLAS Collaboration, *Technical Design Report for the Phase-I Upgrade of the ATLAS TDAQ System*, Tech. rep., CERN, Sep 2013.

47. Boos, E., V. Bunichev, M. Dubinin, L. Dudko, V. Ilyin, A. Kryukov, V. Edneral, V. Savrin, A. Semenov and A. Sherstnev, "CompHEP 4.4: Automatic Computations from Lagrangians to Events", *Nuclear Instruments and Methods in Physics Research Section A*, Vol. 534, pp. 250–259, 2004.

48. Alwall, J., R. Frederix, S. Frixione, V. Hirschi, F. Maltoni, O. Mattelaer, H.-S. Shao, T. Stelzer, P. Torrielli and M. Zaro, "The Automated Computation of Tree-

Level and Next-to-Leading Order Differential Cross Sections, and Their Matching to Parton Shower Simulations", *Journal of High Energy Physics*, Vol. 2014, No. 7, Jul 2014.

49. Sjostrand, T., S. Mrenna and P. Z. Skands, "A Brief Introduction to PYTHIA 8.1", *Computer Physics Communications*, Vol. 178, pp. 852–867, 2008.

50. Ovyn, S., X. Rouby and V. Lemaitre, "Delphes, a Framework for Fast Simulation of a Generic Collider Experiment", *arXiv preprint arXiv:0903.2225*, 2009.

51. Kiryunin, A. E., H. Oberlack, D. Salihagic, P. Schacht and P. Strizenec, "GEANT4 Physics Evaluation with Testbeam Data of the ATLAS Hadronic End-Cap Calorimeter", *Nuclear Instruments and Methods in Physics Research Section A*, Vol. 560, pp. 278–290, 2006.

52. Lampl, W., S. Laplace, D. Lelas, P. Loch, H. Ma, S. Menke, S. Rajagopalan, D. Rousseau, S. Snyder and G. Unal, *Calorimeter Clustering Algorithms: Description and Performance*, Tech. rep., CERN, Geneva, Apr 2008.

53. Cornelissen, T. G., M. Elsing, I. Gavrilenko, J. F. Laporte, W. Liebig, M. Limper, K. Nikolopoulos, A. Poppleton and A. Salzburger, "The Global χ^2 Track Fitter in ATLAS", *Journal of Physics: Conference Series*, Vol. 119, p. 032013, 2008.

54. ATLAS Collaboration, *Improved Electron Reconstruction in ATLAS Using the Gaussian Sum Filter-based Model for Bremsstrahlung*, Tech. rep., CERN, Geneva, May 2012.

55. ATLAS Collaboration, "Electron Reconstruction and Identification in the ATLAS Experiment Using the 2015 and 2016 LHC Proton-Proton Collision Data at $\sqrt{s} =$ 13 TeV", *The European Physical Journal C*, Vol. 79, p. 639. 40 p, Feb 2019.

56. ATLAS Collaboration, *Electron efficiency measurements with the ATLAS detector using the 2015 LHC proton-proton collision data*, Tech. rep., CERN, Geneva, Jun

2016.

57. Aad, G., B. Abbott, J. Abdallah, O. Abdinov, R. Aben, M. Abolins, O. S. AbouZeid, H. Abramowicz, H. Abreu and et al., "Topological Cell Clustering in the ATLAS Calorimeters and Its Performance in LHC Run 1", *The European Physical Journal C*, Vol. 77, No. 7, Jul 2017.

58. Cacciari, M., G. P. Salam and G. Soyez, "The Anti-ktjet Clustering Algorithm", *Journal of High Energy Physics*, Vol. 2008, No. 04, p. 063–063, Apr 2008.

59. Aad, G., T. Abajyan, B. Abbott, J. Abdallah, S. Abdel Khalek, O. Abdinov, R. Aben, B. Abi, M. Abolins and et al., "Jet Energy Measurement and Its Systematic Uncertainty in Proton–Proton Collisions at $\sqrt{s} = 7$ TeV with the ATLAS Detector", *The European Physical Journal C*, Vol. 75, No. 1, Jan 2015.

60. Adams, D. *et al.*, *Recommendations of the Physics Objects and Analysis Harmonisation Study Groups 2014*, Tech. rep., CERN, Geneva, May 2014, accessed in June 2021.

61. ATLAS Collaboration, *ATLAS Collaboration, ATLAS Overlap Removal Tool, 2015*, 2015, `https://gitlab.cern.ch/atlas/athena/tree/master/PhysicsAnalysis/`, accessed in June 2021.

62. Ünel, G. and S. Sekmen, "CutLang: A Particle Physics Analysis Description Language and Runtime Interpreter", *Computer Physics Communications*, Vol. 233, p. 215–236, Dec 2018.

63. Özcan, V. E., *KAHVELab - Boğaziçi University Kandilli Detector, Accelerator and Instrumentation Laboratory*, `http://kahvelab.boun.edu.tr/`, accessed in June 2021.

64. Ünel G., *Repository for CutLang V3*, `https://github.com/unelg/CutLang`, accessed in June 2021.

65. Unel, G., S. Sekmen, A. M. Toon, B. Gokturk, B. Orgen, A. Paul, N. Ravel and J. Setpal, "CutLang v2: Advances in a Runtime-Interpreted Analysis Description Language for HEP Data", *Frontiers in Big Data*, Vol. 4, p. 27, 2021.

66. Franchini, M., T. Novak, M. Sioli, A. Sidoti, G. Carratta, B. P. Kersevan, E. Lytken, K. H. Mankinen, F. Scutti and A. Gorisek, *Search for Type-III Seesaw Heavy Leptons in Multi-lepton Final States Using 139 fb−1 of pp Collisions at $\sqrt{s}$ = 13TeV with the ATLAS Detector*, Tech. rep., CERN, Geneva, Feb 2019.

67. ATLAS Collaboration, *Athena*, Apr. 2019, `https://doi.org/10.5281/zenodo.2641997`.

68. Gleisberg, T., S. Höche, F. Krauss, M. Schönherr, S. Schumann, F. Siegert and J. Winter, "Event Generation with SHERPA 1.1", *Journal of High Energy Physics*, Vol. 2009, No. 02, p. 007–007, Feb 2009.

69. Ball, R. D. *et al.*, "Parton Distributions for the LHC Run II", *Journal of High Energy Physics*, Vol. 04, p. 040, 2015.

70. Alioli, S., P. Nason, C. Oleari and E. Re, "A General Framework for Implementing NLO Calculations in Shower Monte Carlo Programs: the POWHEG BOX", *Journal of High Energy Physics*, Vol. 06, p. 043, 2010.

71. Cowan, G., K. Cranmer, E. Gross and O. Vitells, "Asymptotic Formulae for Likelihood-based Tests of New Physics", *The European Physical Journal C*, Vol. 71, No. 2, Feb 2011.

72. ATLAS Collaboration, *TRExFitter GitLab Repository*, `https://gitlab.cern.ch/TRExStats/TRExFitter`, accessed in June 2021.

73. L3 Collaboration, "Search for Heavy Neutral and Charged Leptons in e+e− Annihilation at LEP", *Physics Letters B*, Vol. 517, No. 1, pp. 75–85, 2001.

74. Boos, E., V. Bunichev, M. Dubinin, L. Dudko, V. Edneral, V. Ilyin, A. Kryukov, V. Savrin, A. Semenov and A. Sherstnev, "CompHEP 4.4—Automatic Computations from Lagrangians to Events", *Nuclear Instruments and Methods in Physics Research Section A: Accelerators, Spectrometers, Detectors and Associated Equipment*, Vol. 534, No. 1-2, p. 250–259, Nov 2004.

APPENDIX A: ANALYSIS ADL FILE USED IN CutLang

The following is the contents of the ADL file used during this study. Object and function definitions along with event selection criteria, output histograms and many more options are all controlled by this file.

```
TRGm = 0 #      muon Trigger Type: 0=dont trigger, 1=1st trigger (data)
    2=2nd trigger (MC)
TRGe = 2 # electron Trigger Type: 0=dont trigger, 1=1st trigger (data)
    2=2nd trigger (MC)
#SkipEffs = 1 # 0: show effieciencies 1: do not
SkipHistos = 1 # 0: plot histograms 1: do not

######## OBJECT DEFINITONS
object goodELE : ELE
select AbsEta(ELE_) < 2.47  # max pseudorapidity of electrons
select AbsEta(ELE_) ][ 1.37 1.52  # exclude pseudorapidity of electrons
    (support section of ATLAS detector)
select Pt(ELE_) > 10.0  # min pt of electrons
select LEPTIGHT(ELE_) == 0 # isolation and identification criteria

object goodMUO : MUO
select Pt(MUO_) > 10.0  # min pt of muons
select AbsEta(MUO_) < 2.5  # max pseudorapidity of electrons
select LEPTIGHT(MUO_) == 0 # isolation and identification criteria

object goodJET : JET
select Pt(JET_) > 20.0  # min pt of jets
select AbsEta(JET_) < 2.5  # max pseudorapidity of electrons

object goodleptons : Union( goodELE, goodMUO )  # goodleptons  involve
    both goodELE and goodMUO

define      goodJETA = goodJET_-1  # unlabeled jets
define      goodJETB = goodJET_-2  # will be defined in the ~= selections
```

```
define      goodLEPA = goodleptons_-3
define      goodLEPB = goodleptons_-4
define      goodLEPC = goodleptons_-5

###### USER DEFINITIONS
define      Zreco : goodLEPA goodLEPB
define      pdgidDiff : abs(abs(PDGID(goodLEPA)) - abs(PDGID(goodLEPB)))
define      Zsameflavor: (abs( q(Zreco) ) + pdgidDiff)*100000 +
   abs(m(Zreco) - 91.0) + 0*pt( goodLEPC )
define      LeZ : Zreco goodLEPC
define      Wreco : goodJETA goodJETB
define      LeW : Wreco METLV_0
define      HT : { goodJETA }Pt + { goodJETB }Pt
define      HTJ : fHT(goodJET)
define      METsig : MET / sqrt( HTJ + pt(goodLEPA) + pt(goodLEPB) +
   pt(goodLEPC) )
define      METplusHT : MET + HT
define      diffLEp :  { goodLEPA }Pt - { goodLEPB }Pt
define      LLdiff = abs( m(LeZ) -m(LeW) )

###### EVENT SELECTION
algo  preselection
select      ALL             # to count all events
select      XSLumiCorrSF
select      Size(goodMUO) >= 0
select      Size(goodELE) >= 0
select      Size(goodleptons) >= 1
select      Size(goodleptons) >= 2
select      Size(goodleptons) >= 3
select      Size(goodleptons) == 3
Sort        {goodleptons_ }Pt descend
histo       preslepleadpt , "Leading Lepton Pt [GeV]", 70, 0, 700, {
   goodleptons_0 }Pt
histo       presnlepleadpt , "Next to Leading Lepton Pt [GeV]", 70, 0,
   700, { goodleptons_1 }Pt
histo       presnnlepleadpt , "pT of Lepton with the Lowest pt [GeV]",
   70, 0, 700, { goodleptons_2 }Pt
```

```
select      pt(goodleptons_0) > 40.0
select      pt(goodleptons_1) > 40.0
select      Size(goodJET) >= 2
select      Size(goodELE) == 1 OR Size(goodELE) == 3
select      Zsameflavor ~= 0.0
select      pdgidDiff == 0
select      q(Zreco) == 0
histo       presZmass , "Mass of reconstructed Z [GeV]", 90, 0, 180, m(
    Zreco )
select      m(Zreco) [] 85 95
select      abs(PDGID(goodLEPC)) == 11
select      m(Wreco) ~= 80
histo       presWmass , "Mass of reconstructed W [GeV]", 80, 0, 400,
    m(Wreco)
select      m(Wreco) [] 50 110

##### End of pre-selection histograms
histo     postpremet , "MET [GeV]", 50, 0, 500, { METLV_0 }Pt
histo     postpremetsig , "METsig [GeV]", 75, 0, 15, METsig
histo     postpreht , "Total PT of W jets [GeV]", 70, 0, 700, HT
histo     postpremetplusht , "MET + pT of W candidate jets [GeV]", 90,
    0, 900, METplusHT
histo     postprelepleadpt , "Leading Lepton Pt [GeV]", 60, 0, 600, {
    goodleptons_0 }Pt
histo     postprelepnleadpt , "Next to Leading Lepton Pt [GeV]", 60, 0,
    600, { goodleptons_1 }Pt
histo     postprelepnnleadpt , "pT of Lepton with the Lowest pt [GeV]",
    60, 0, 600, { goodleptons_2 }Pt
histo     postprelepapt0 , "Leading Z candidate lepton pT [GeV]", 60, 0,
    600, { goodLEPA }Pt
histo     postprelepbpt0 , "Next to Leading Z candidate lepton pt
    [GeV]", 60, 0, 600, { goodLEPB }Pt
histo     postprelepcpt0 , "pT of Electron from Le->Ze [GeV]", 60, 0,
    600, { goodLEPC }Pt
histo     postprelepaeta , "Leading Z candidate lepton eta", 60, -3, 3,
    { goodLEPA }Eta
histo     postprelepbeta , "Next to Leading Z candidate lepton eta", 60,
```

```
    -3, 3, { goodLEPB }Eta
histo      postprelepceta , "eta of Electron from Le->Ze ", 60, -3, 3, {
    goodLEPC }Eta
histo      postprelepaphi , "Leading Z candidate lepton phi", 70, -3.5,
    3.5, { goodLEPA }Phi
histo      postprelepbphi , "Next to Leading Z candidate lepton phi", 70,
    -3.5, 3.5, { goodLEPB }Phi
histo      postprelepcphi , "phi of Electron from Le->Ze ", 70, -3.5,
    3.5, { goodLEPC }Phi
histo      postprelepangdist , "Angular Distance between the Z candidates
    ", 50, 0.0, 4.5, { goodLEPA , goodLEPB }dR
histo      postpreeZang , "Angular Distance between the Reconstructed Z
    and Remaining Electron", 70, 0.0, 6.5, { goodLEPC , Zreco }dR
histo      postpreWpt , "Reconstructed W pT [GeV]", 60, 0, 600, { Wreco
    }Pt
histo      postpreZpt , "Reconstructed Z pT [GeV]", 60, 0, 600, { Zreco
    }Pt
histo      postpreWeta , "Reconstructed W eta", 55, -5.5, 5.5, { Wreco
    }Eta
histo      postpreZeta , "Reconstructed Z eta", 55, -5.5, 5.5, { Zreco
    }Eta
histo      postpreWphi , "Reconstructed W phi", 70, -3.5, 3.5, { Wreco
    }Phi
histo      postpreZphi , "Reconstructed Z phi", 70, -3.5, 3.5, { Zreco
    }Phi

select     METsig > 1.0
select     abs ( { goodLEPC , Zreco }dR ) < 3.1
select     HT > 60.0
select     METplusHT > 120.0

histo      sigreglldrdiff1 ,"Angular Distance between Le from W and Z
    Channels",70, 0, 7,{ LeW , LeZ }dR
histo      sigreglezpt1 , "pT of Le from Z channel [GeV]", 65, 0, 650, {
    LeZ }Pt
histo      sigreglewpt1 , "pT of Le from W channel [GeV]", 65, 0, 650, {
    LeW }Pt
```

```
histo      sigregLeZeta1 , "eta of Le from Z channel", 80, -4.0, 4.0, {
   LeZ }Eta
histo      sigregLeWeta1 , "eta of Le from W channel", 80, -4.0, 4.0, {
   LeW }Eta
histo      sigregLeZphi1 , "phi of Le from Z channel", 70, -3.5, 3.5, {
   LeZ }Phi
histo      sigregLeWphi1 , "phi of Le from W channel", 70, -3.5, 3.5, {
   LeW }Phi
histo      sigregLeZm1 , "Reconstructed Mass of Le from Z channel [GeV]",
   90, 80, 530, m(LeZ)
histo      sigregLeWm1 , "Reconstructed Mass of Le from W channel [GeV]",
   70, 50, 750, m(LeW)
histo      sigregllmassdiff1 , "Mass difference between
   Le's",60,0,600,LLdiff
histo      sigreglepcpt , " pT of Electron from Le->Ze [GeV]", 50, 0,
   500, { goodLEPC }Pt
histo      sigreglepceta , "eta of Electron from Le->Ze", 50, -3, 3, {
   goodLEPC }Eta
histo      sigreglepcphi , "phi of Electron from Le->Ze", 70, -3.5, 3.5,
   { goodLEPC }Phi

select     { LeW , LeZ }dR [] 2.6 4.1
select     pt(LeW) > 40.0
select     pt(LeZ) > 40.0
select     LLdiff < 160.0
select     pt(goodLEPC) > 40.0

##### End of Signal Region histograms
histo      postsigregllmassdiff1 , "Mass difference between Le's
   [GeV]",90,0,180, LLdiff
histo      postsigregLeZm2 , "Reconstructed Mass of Le from Z channel
   [GeV]", 80, 50, 450, m(LeZ)
histo      postsigregLeWm2 , "Reconstructed Mass of Le from W channel
   [GeV]", 80, 50, 450, m(LeW)
histo      postsigreglezpt1 , "pT of Le from Z channel [GeV]", 60, 40,
   640, { LeZ }Pt
histo      postsigreglewpt1 , "pT of Le from W channel [GeV]", 60, 40,
```

```
    640, { LeW }Pt
histo      postsigregLeZeta1 , "eta of Le from Z channel", 70, -3.5, 3.5,
    { LeZ }Eta
histo      postsigregLeWeta1 , "eta of Le from W channel", 70, -3.5, 3.5,
    { LeW }Eta
histo      postsigregLeZphi1 , "phi of Le from Z channel ", 70, -3.5,
    3.5, { LeZ }Phi
histo      postsigregLeWphi1 , "phi of Le from W channel", 70, -3.5, 3.5,
    { LeW }Phi
```

APPENDIX B: ADDITIONAL HISTOGRAMS FROM ANALYSIS

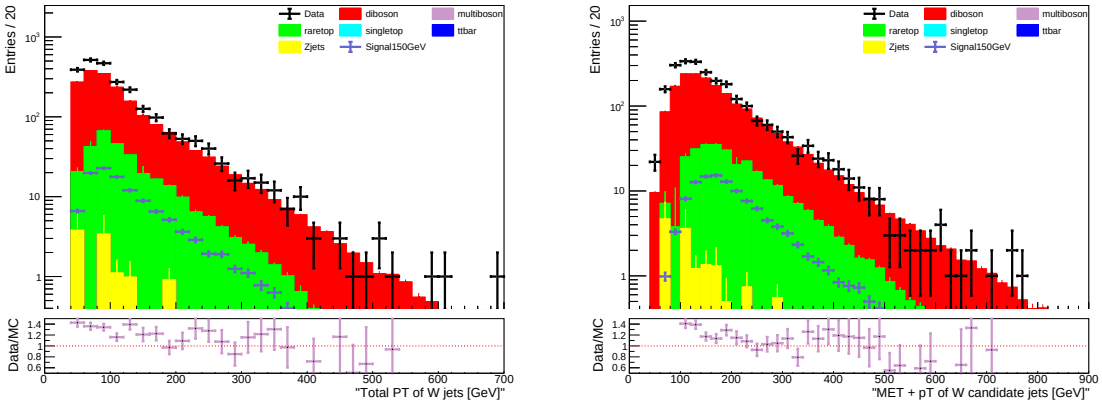

Figure B.1. Sum of W candidate p_T's and $E_T^{miss.}$ added together with W candidate p_T's after the pre-selection criteria.

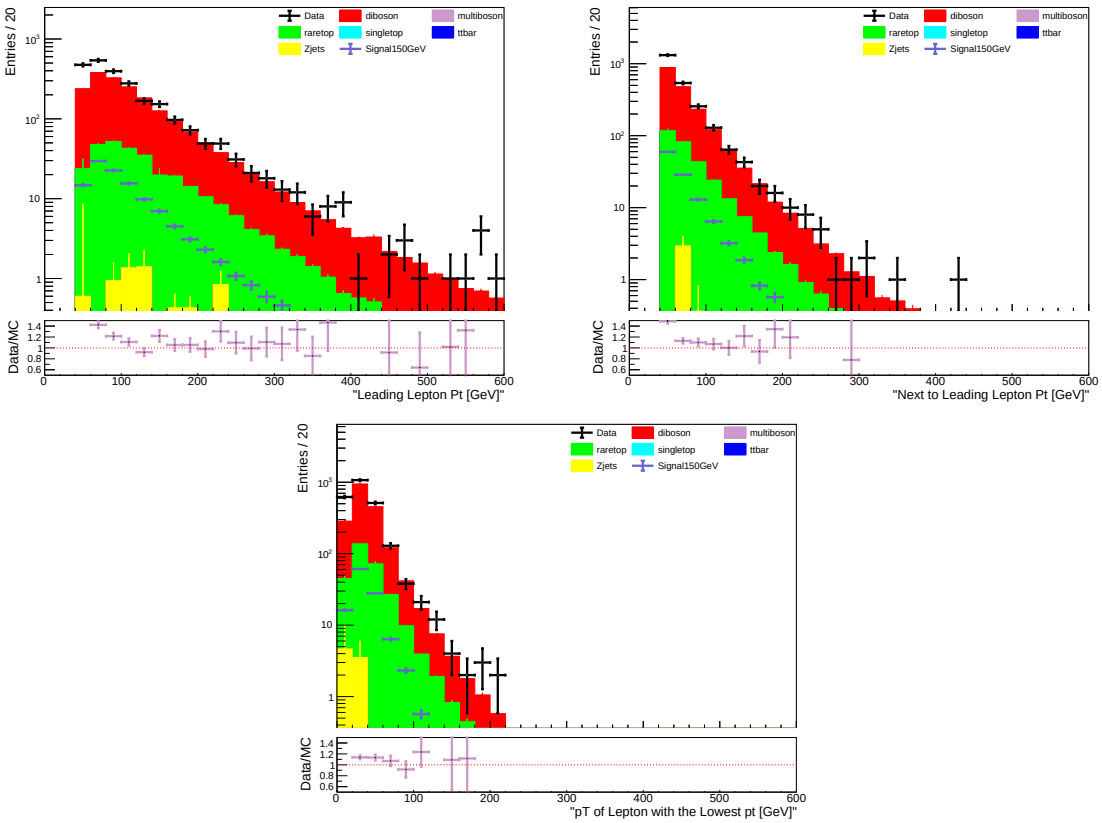

Figure B.2. p_T distributions of the leptons after the pre-selection criteria.

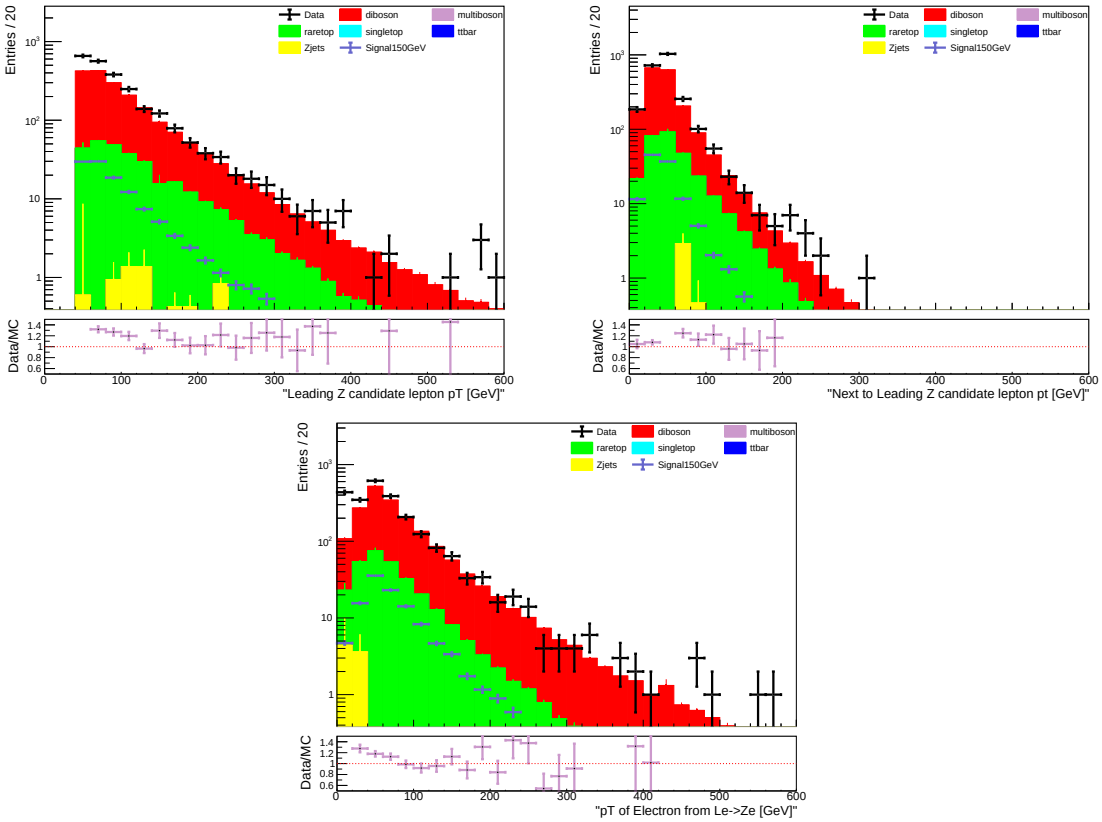

Figure B.3. p_T distributions of the Z candidate leptons and the electron of $L_e \to Ze$ decay after the pre-selection criteria.

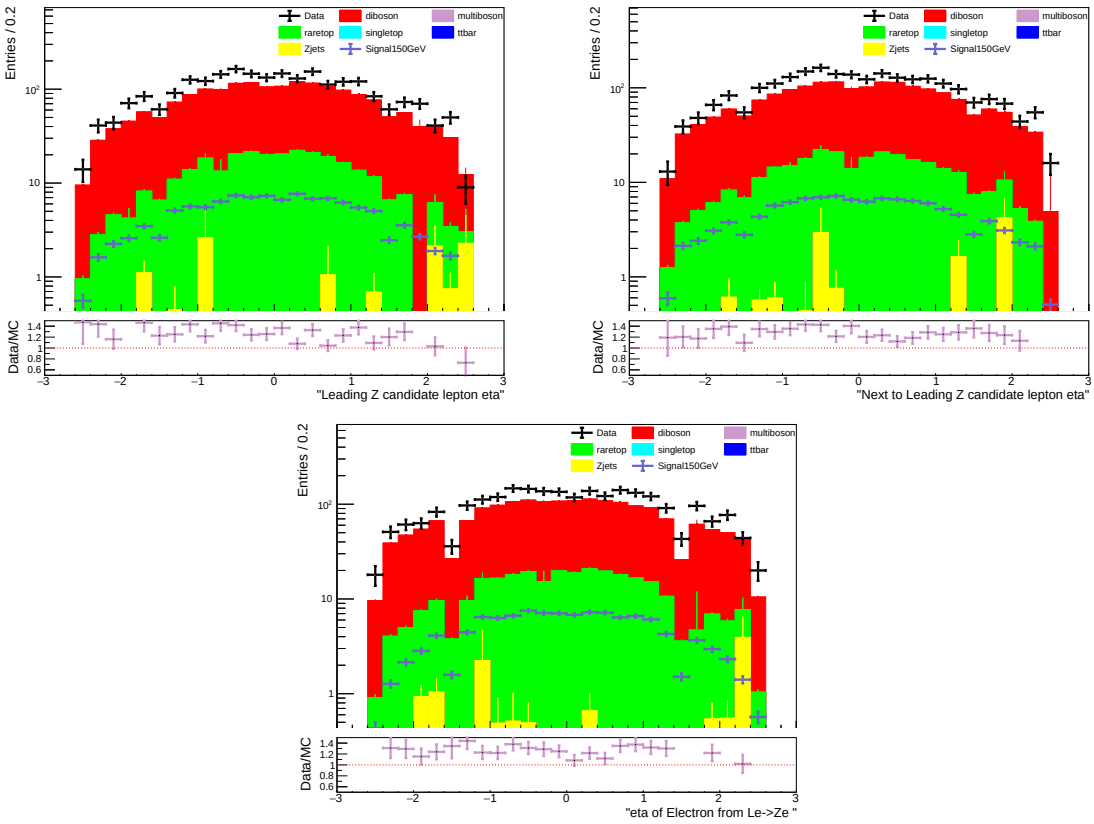

Figure B.4. η distributions of the Z candidate leptons and the electron of $L_e \to Ze$ decay after the pre-selection criteria.

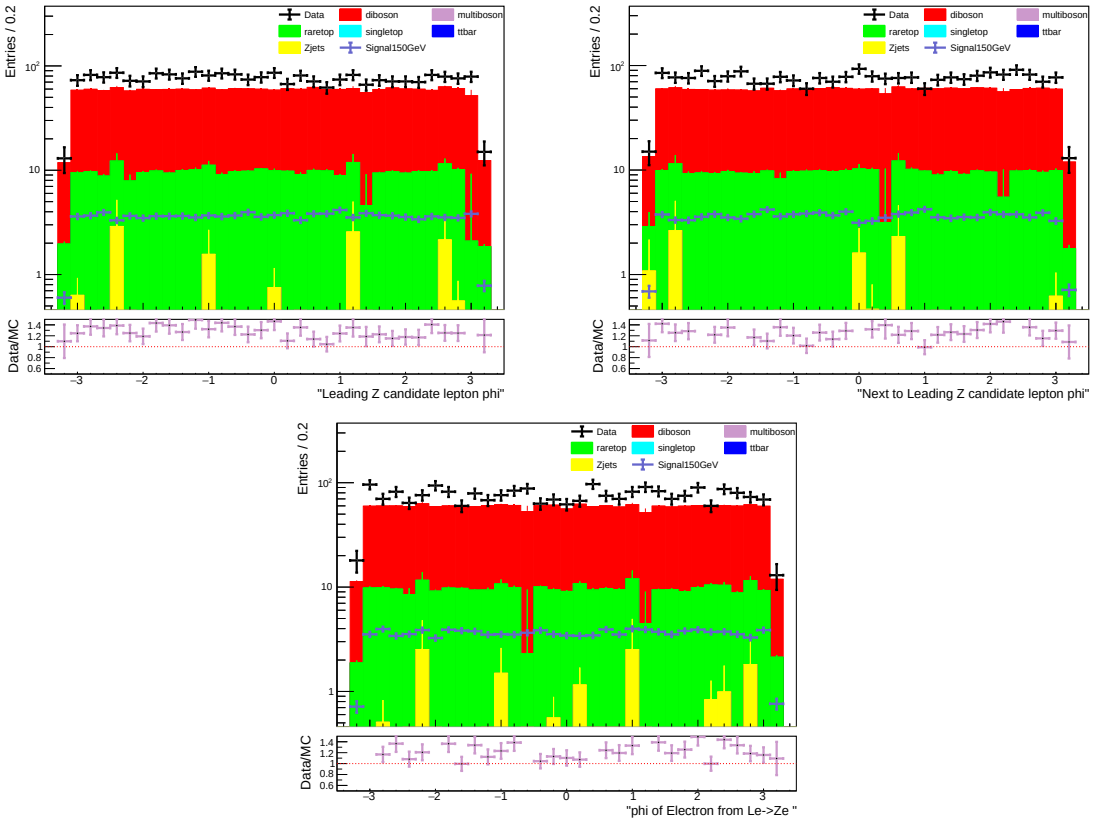

Figure B.5. ϕ distributions of the Z candidate leptons and the electron of $L_e \rightarrow Ze$ decay after the pre-selection criteria.

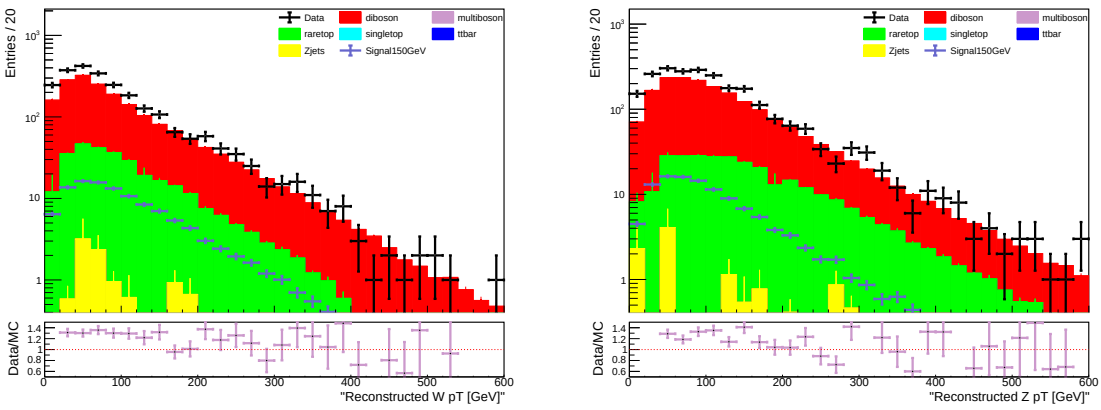

Figure B.6. p_T distributions of the reconstructed Z and W after the pre-selection criteria.

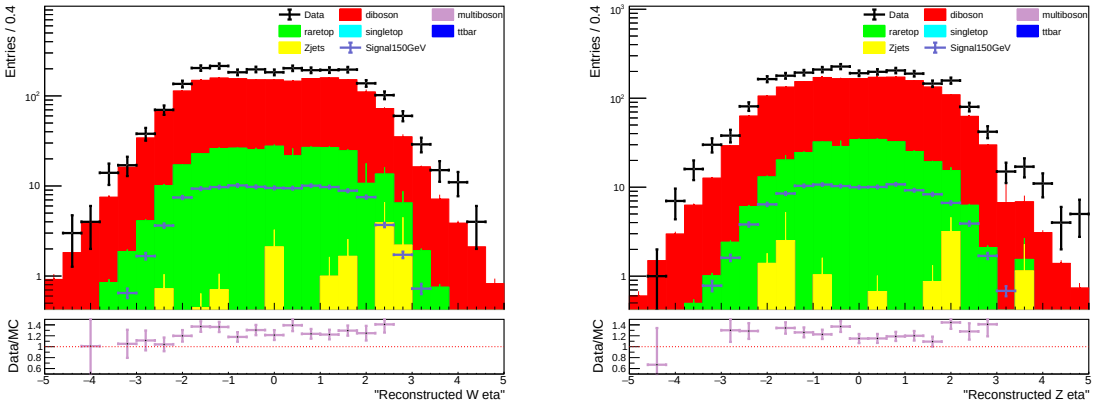

Figure B.7. η distributions of the reconstructed Z and W after the pre-selection criteria.

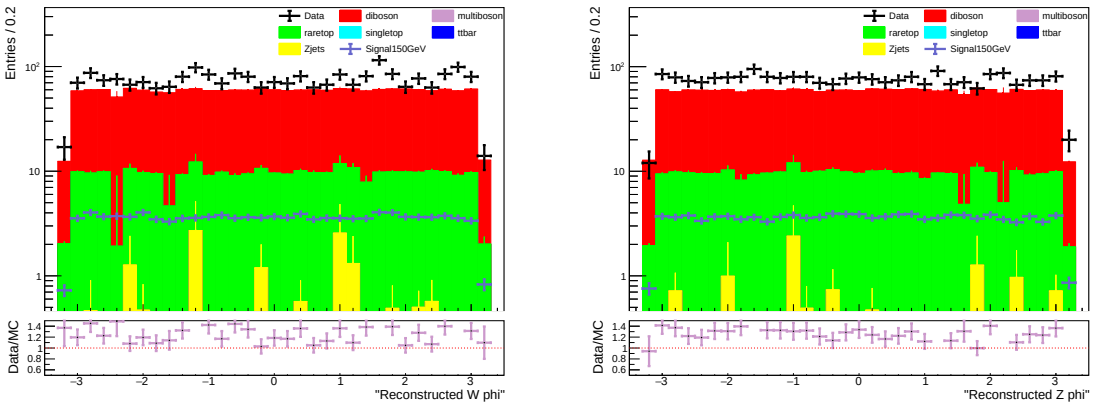

Figure B.8. ϕ distributions of the reconstructed Z and W after the pre-selection criteria.

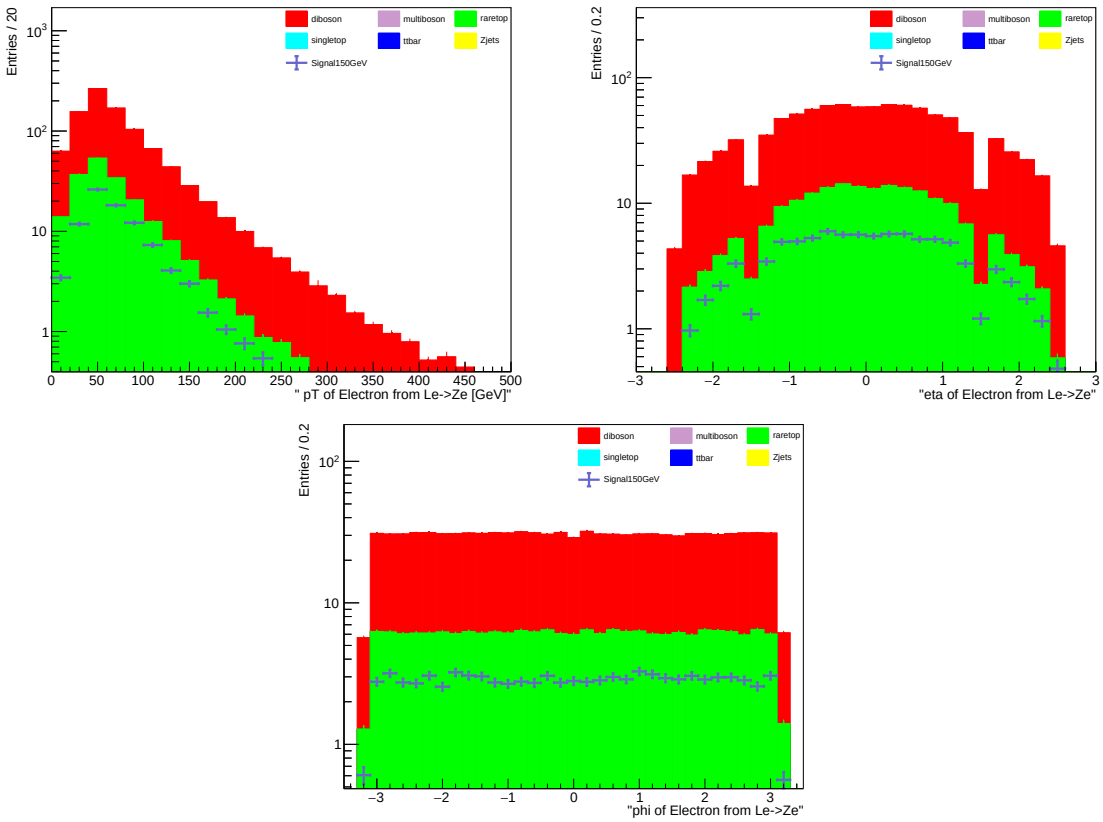

Figure B.9. p_T, η and ϕ distributions of the electron of $L_e \to Ze$ decay after the 4^{th} signal region selection.

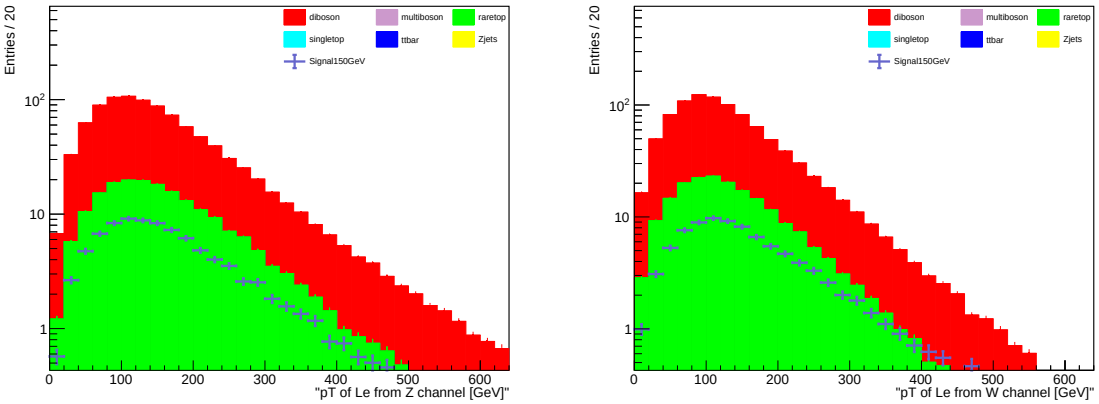

Figure B.10. p_T of reconstructed L_e's after the 4^{th} signal region selection.

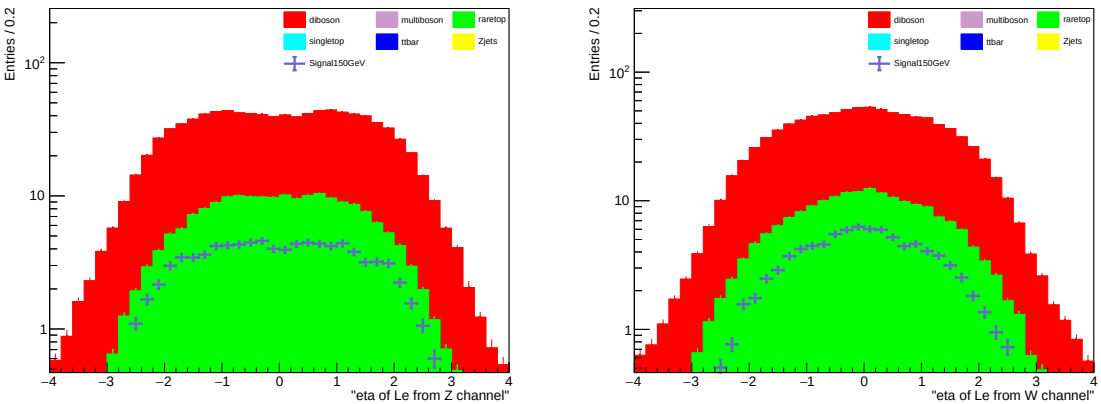

Figure B.11. η of reconstructed L_e's after the 4^{th} signal region selection.

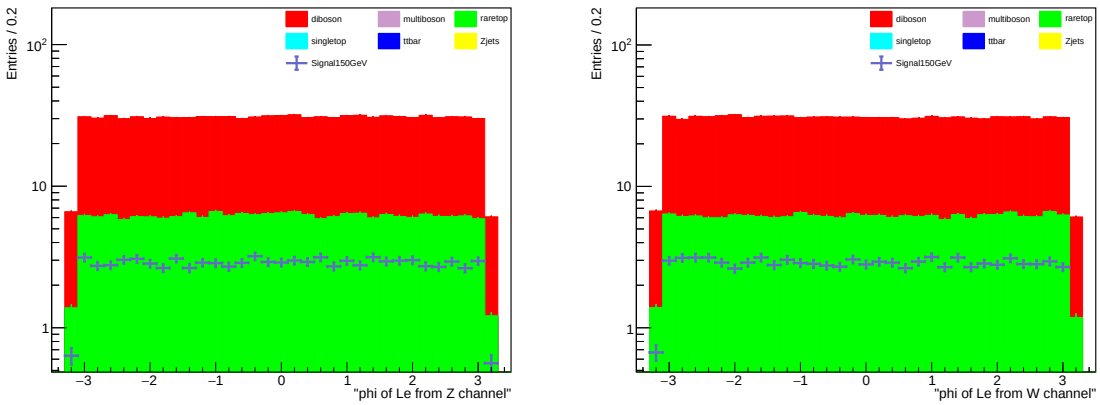

Figure B.12. ϕ of reconstructed L_e's after the 4^{th} signal region selection.